Monthly Notices
of the
ROYAL ASTRONOMICAL SOCIETY

MNRAS **496,** 1620–1637 (2020)
Advance Access publication 2020 June 10

doi:10.1093/mnras/staa1619

Swirls of FIRE: spatially resolved gas velocity dispersions and star formation rates in FIRE-2 disc environments

Matthew E. Orr [1]★ Christopher C. Hayward [2] Anne M. Medling [3,4]† Alexander B. Gurvich [5] Philip F. Hopkins [1] Norman Murray,[6] Jorge L. Pineda,[7] Claude-André Faucher-Giguère [5] Dušan Kereš,[8] Andrew Wetzel [9] and Kung-Yi Su[1,2]

[1]*TAPIR, Mailcode 350-17, California Institute of Technology, Pasadena, CA 91125, USA*
[2]*Center for Computational Astrophysics, Flatiron Institute, 162 Fifth Avenue, New York, NY 10010, USA*
[3]*Ritter Astrophysical Research, Center University of Toledo, Toledo, OH 43606, USA*
[4]*Research School for Astronomy & Astrophysics, Australian National University, Canberra, ACT 2611, Australia*
[5]*CIERA and Department of Physics and Astronomy, Northwestern University, 1800 Sherman Ave., Evanston, IL 60201, USA*
[6]*Canadian Institute for Theoretical Astrophysics, 60 St George Street, University of Toronto, Toronto, ON M5S 3H8, Canada*
[7]*Jet Propulsion Laboratory, California Institute of Technology, 4800 Oak Grove Drive, Pasadena, CA 91109-8099, USA*
[8]*Department of Physics, Center for Astrophysics and Space Science, University of California at San Diego, 9500 Gilman Drive, La Jolla, CA 92093, USA*
[9]*Department of Physics, University of California, Davis, CA 95616, USA*

Accepted 2020 May 28. Received 2020 May 27; in original form 2019 October 30

ABSTRACT

We study the spatially resolved (sub-kpc) gas velocity dispersion (σ)–star formation rate (SFR) relation in the FIRE-2 (Feedback in Realistic Environments) cosmological simulations. We specifically focus on Milky Way-mass disc galaxies at late times ($z \approx 0$). In agreement with observations, we find a relatively flat relationship, with $\sigma \approx 15$–$30\,\mathrm{km\,s^{-1}}$ in neutral gas across 3 dex in SFRs. We show that higher dense gas fractions (ratios of dense gas to neutral gas) and SFRs are correlated at constant σ. Similarly, lower gas fractions (ratios of gas to stellar mass) are correlated with higher σ at constant SFR. The limits of the σ–Σ_{SFR} relation correspond to the onset of strong outflows. We see evidence of 'on-off' cycles of star formation in the simulations, corresponding to feedback injection time-scales of 10–100 Myr, where SFRs oscillate about equilibrium SFR predictions. Finally, SFRs and velocity dispersions in the simulations agree well with feedback-regulated and marginally stable gas disc (Toomre's $Q = 1$) model predictions, and the simulation data effectively rule out models assuming that gas turns into stars at (low) constant efficiency (i.e. 1 per cent per free-fall time). And although the simulation data do not entirely exclude gas accretion/gravitationally powered turbulence as a driver of σ, it appears to be subdominant to stellar feedback in the simulated galaxy discs at $z \approx 0$.

Key words: ISM: kinematics and dynamics – galaxies: evolution – galaxies: ISM – galaxies: kinematics and dynamics – galaxies: spiral – galaxies: star formation.

1 INTRODUCTION

Star formation in the Local Universe (at $z \approx 0$) is dominated by spiral galaxies of approximately Milky Way-mass (stellar masses of $\sim 10^{10}$–10^{11} $\mathrm{M}_{\odot}$, Brinchmann et al. 2004; Behroozi, Wechsler & Conroy 2013). A hallmark of these galaxies at late times is relatively constant steady star formation in the galaxy disc over the last several billion years (Ma et al. 2017; Simons et al. 2017). Understanding how star formation and the interstellar medium (ISM) interact in disc environments is therefore crucial to understanding how these galaxies have evolved, and continue to grow.

Observationally, star formation in galaxies has often been studied through the lens of the Kennicutt–Schmidt (KS) and Elmegreen–Silk (ES) relations, both empirical star formation scaling relations relating gas surface densities Σ_{gas}, and gas surface densities times the local orbital dynamical time $\Sigma_{\mathrm{gas}}\Omega$, to the star formation surface density Σ_{SFR}, respectively, to probe the connections between local gas masses and star formation (Kennicutt 1989, and see Kennicutt & Evans 2012 for a recent review). The scatter seen in the KS and ES relations have long been viewed as 'the weather' of variations in

★ E-mail: meorr@caltech.edu
† Hubble Fellow.

local conditions and differing resulting star formation equilibria (Bigiel et al. 2008; Leroy et al. 2008, 2013). However, the KS and ES relations themselves do not directly speak to the *dynamical* state of the gas in galaxies, relating only the surface densities of gas to star formation rates (SFRs). And so theoretical work has been afforded significant leeway in explaining the origins of these star formation scaling relations, from being the direct consequence of stellar feedback, to being purely a result of gas dynamics and migration in galaxies (Faucher-Giguere, Quataert & Hopkins 2013; Krumholz & Burkhart 2016).

Theoretical work has shown these relations can be understood on average by treating star formation as a self-regulating process (Thompson, Quataert & Murray 2005; Ostriker & Shetty 2011; Faucher-Giguere et al. 2013; Hayward & Hopkins 2017). The hierarchy of time-scales involved in galaxies provided motivation for this: star formation, and the bulk of stellar feedback, occurs on the time-scale of a few million years or less (tens at most), but the dynamical times of galaxies can be on the order of 100 Myr. If galaxies are to have long-lived coherent structures (e.g. spiral arms), star formation must either be on-average in equilibrium with those structures, or be unable to greatly affect them.

Recent work exploring star formation as a non-equilibrium process on the scales of giant molecular clouds (GMCs, $\gtrsim 100$ pc) has argued for the importance of local gas dynamics (e.g. gas turbulence) in producing both the scatter and normalization in star formation scaling relations like KS (Benincasa et al. 2016; Sparre et al. 2017; Torrey et al. 2017; Orr, Hayward & Hopkins 2019). Work by Torrey et al. (2017) to understand how the outflows and 'breathing modes' of central molecular regions are tied to star formation shows that non-equilibrium SFRs, on time-scales of tens of millions of years, arise naturally from the competition between the stellar feedback and dissipative dynamical processes. Further works by Benincasa et al. (2016) and Orr et al. (2019) have explored the dynamical and SFR responses of the ISM in disc environments to changing velocity dispersions and feedback injection, on the time-scales of tens of Myr.

Much work on star formation in both equilibrium and non-equilibrium contexts has focused on the stability of gas in galaxies against gravitational fragmentation and collapse. Gas velocity dispersions σ are seen as a key driver of gravitational stability and a measure of the dynamical state of gas in galaxy discs, with dense gas velocity dispersions (observationally, line-widths from molecular gas tracers like CO or HCN) being tied to the degree of turbulent support within the discs. The connection between σ and stability is most explicit when gas stability is calculated using the (modified) Toomre-Q parameter (Toomre 1964), having a form similar to

$$\tilde{Q}_{\rm gas} \equiv \frac{\sqrt{2}\sigma_z \Omega}{\pi G(\Sigma_{\rm gas} + \gamma \Sigma_\star)} \, , \tag{1}$$

where σ_z is the vertical (line-of-sight) velocity dispersion in the gas,[1] Ω the dynamical angular velocity ($\Omega \equiv v_c/R$), and $(\Sigma_{\rm gas} + \gamma \Sigma_\star)$ being the effective disc surface density, where $\Sigma_{\rm gas}$ is the neutral (atomic + molecular) gas surface density and the $\gamma \Sigma_\star$ represents the fraction of the stellar component within the gas disc scale height (and thus contributing to the self-gravity of the disc).[2]

For gas in galaxies with $\tilde{Q}_{\rm gas} \lesssim 1$, there is insufficient turbulent support (σ) to prevent fragmentation and gravitational collapse. This gas collapses to form stars, removing it from the gas reservoir. In the feedback-regulated framework, those stars then inject feedback to the remaining gas to stabilize it. On the other hand, gas with $\tilde{Q}_{\rm gas} \gg 1$ is likely to be dynamically expanding or in the midst of an outflow event. In the event that this gas is not being actively driven to larger values of $\tilde{Q}_{\rm gas}$, it is expected that the gas dissipates its turbulence rapidly on a disc crossing time, driving to $\tilde{Q}_{\rm gas} = 1$. And so, for the purposes of supersonically turbulent discs, we expect that gas ought to converge to a $\tilde{Q}_{\rm gas} \approx 1$.

The rate at which marginally unstable gas ($\tilde{Q}_{\rm gas} \lesssim 1$) in galaxies ought to form stars is theoretically uncertain. Some feedback-regulation arguments, for example that feedback from young stars balances the gravitational weight of the ISM, are completely agnostic to the velocity dispersions or specific value of Toomre-Q (Ostriker & Shetty 2011). And so, in spite of good arguments for $\tilde{Q}_{\rm gas} \rightarrow 1$ convergence on large scales, we are still left with conflicting evidence and predictions for how gas turbulence (velocity dispersions/observed line-widths) is sourced and whether it is a direct consequence, or cause of, local SFRs (see Section 4.2 for a more in-depth discussion). That of the quantities involved in predicting $\tilde{Q}_{\rm gas}$, only σ appreciably evolves on time-scales $\lesssim$ 100 Myr (barring significant gas inflows/outflows) highlights the importance of understanding how velocity dispersions and star formation connect.

Much of the work understanding the velocity dispersion structure of gas in local galaxies and their relationship with local SFRs has investigated the HII regions of those galaxies (Larson 1981; Gallagher & Hunter 1983; Rozas et al. 1998, 2007; Zhou et al. 2017), due in part to the relative difficulty in adequately measuring at high-velocity resolution the velocity structure of the colder, fainter dense molecular gas tracers like CO or HCN. Modern surveys are just now beginning to report on the galaxy-wide, spatially resolved velocity structure and surface density distributions in the cold, dense molecular gas (Leroy et al. 2017; Gallagher et al. 2018a,b; Sun et al. 2018; Querejeta et al. 2019). Recent work has focused on how dense gas fractions and the mid-plane pressure of the ISM correlate with star formation efficiencies, and whether or not variations in these quantities can explain the variations seen in SFRs across the galaxies as a whole.

Cosmological zoom-in simulations are now beginning to resolve the ISM on scales within GMC complexes, with subparsec spatial resolution and mass resolutions reaching sub-10^3 $M_\odot$ (Hopkins et al. 2014; Wetzel et al. 2016; Hopkins et al. 2018). Given the ability to resolve ISM dynamics on the scales within star-forming regions, recent work by Orr et al. (2018) has explored the spatially resolved properties of the Kennicutt-Schmidt relation and its dependences on local gas properties in the FIRE simulations. Another investigation of the FIRE suite by El-Badry et al. (2018) investigated the kinematic and morphological properties of gas within galaxies. However, neither study explicitly explored the connection between the spatially resolved gas kinematics (velocity dispersions) and the local SFRs.

[1] It is often assumed that the turbulence field is roughly isotropic on a disc scale height, so the in-plane turbulence in a disc (used for the 'classical' Toomre-Q parameter) is equivalent to the line-of-sight component, thus $\sigma_R \approx \sigma_z$.

[2] For all subsequent calculations of $\tilde{Q}_{\rm gas}$ in this work, we calculate the γ factor assuming that the stellar component has an exponential scale height, and thus is $\gamma = 1 - \exp(-\sigma_{z,\,\rm gas}/\sigma_{z,\,\star})$, to simplify direct calculations of this factor in comparisons with observations.

Table 1. Summary of $z \approx 0$ properties of the FIRE-2 Milky Way-like galaxies used in this work.

Name	$\log(\frac{M_\star}{M_\odot})$	$\log(\frac{M_{gas}}{M_\odot})$	$\frac{R_{\star,1/2}}{kpc}$	$\frac{R_{gas,1/2}}{kpc}$	$\frac{v_c}{km\,s^{-1}}$ [a]
m12b	10.8	10.3	2.7	9.4	266
m12c	10.7	10.3	3.4	8.6	232
m12f	10.8	10.4	4.0	11.6	248
m12i	10.7	10.3	2.9	9.8	232
m12m	10.9	10.4	5.6	10.2	283
m12r	10.2	10.0	4.7	9.9	156
m12w	10.6	9.8	3.1	3.1	244

Notes. All quantities measured within a 30 kpc cubic aperture.
[a]Circular velocities evaluated at $R_{gas,\,1/2}$.

In this work, we explore the relationship between various spatially resolved measures of gas velocity dispersion and SFRs using the FIRE-2 cosmological zoom-in simulations. We explore the dependences of the velocity dispersions and SFRs in Milky Way-like disc environments on various local gas properties, disc conditions, and recent star formation histories. We compare the FIRE simulations where possible with spatially resolved observational data sets. Through these means, we test the predictions of several classes of star formation theories that connect gas velocity dispersions/supersonic turbulence with local SFRs and gas stability.

2 SIMULATIONS AND ANALYSIS METHODS

2.1 FIRE-2 simulations

We use the Latte suite of FIRE-2 cosmological zoom-in simulations of isolated MW/M31-mass galaxies, introduced in Wetzel et al. (2016) and Hopkins et al. (2018), including seven galaxies selected to have dark-matter halo masses of $M_{200m} = 1 - 2 \times 10^{12}$ M$_\odot$ at $z = 0$, and no other halo of similar mass within $5R_{200m}$. We selected two of these haloes (**m12w** and **m12r**) to contain an LMC-mass satellite subhalo in the initial dark matter-only simulation (see Samuel et al. 2020). They were run with the gravity + hydrodynamics code GIZMO (Hopkins 2015). Specifically, the simulations were run with a mesh-free Lagrangian Godunov (meshless finite mass, MFM) method. A brief summary of the $z \approx 0$ properties of the galaxy simulations are included in Table 1. These simulations all have a minimum baryonic particle mass of $m_{b,\,min} = 7100$ M$_\odot$, and minimum adaptive force softening lengths <1 pc. As the softening lengths are adaptive, it is useful to note that the typical/median softening length within the disc in one of the runs at $z = 0$, **m12i**, is $h \sim$ 20–40 pc (at $n \sim 1$ cm^{-3}). The minimum length scales considered in this work are hundreds of parsecs, and so are about three orders of magnitude above the minimum resolvable scales in the simulations. All of the simulations employ a standard flat ΛCDM cosmology with $h \approx 0.7$, $\Omega_M = 1 - \Omega_\Lambda \approx 0.27$, and $\Omega_b \approx 0.046$.

The star formation prescription in the FIRE-2 simulations is described in more detail in Hopkins et al. (2018), however, to reiterate here: star formation occurs on a free-fall time in gas which is dense ($n > 10^3$ cm^{-3}), molecular [per the Krumholz & Gnedin (2011) empirical fit for molecular gas fractions as a function of local gas column density], self-gravitating (viral parameter $\alpha_{vir} < 1$) and Jeans-unstable below the resolution scale.

Once a star particle is formed, it is treated as a single stellar population with known age, metallicity, and mass. We explicitly follow feedback from supernovae (Type Ia and II), stellar mass loss (OB/AGB-star winds), photoionization and photoelectric heating, and radiation pressure. Detailed descriptions of these physics and their implementation can be found in Hopkins et al. (2018). All feedback quantities are taken from standard stellar population models (STARBURST99, Leitherer et al. 1999), assuming a Kroupa 2002 IMF.

2.2 Mapping out FIRE-2: resolved 'observations' of the simulations

We generate mock observational maps from a set of snapshots with $z \lesssim 0.1$ in the manner of Orr et al. (2018), by projecting the galaxies face-on with respect to the stellar angular momentum, then binning star particles and gas elements into square pixels[3] with side lengths (i.e. 'pixel sizes') 250–750 pc. The maps themselves are 30 kpc on a side, integrating gas and stars within ±15 kpc of the galaxy mid-plane (to exclude line-of-sight projections of other galaxies within the larger cosmological box).

We generate SFR tracers analogous to observational measures of star formation by calculating the average SFRs over the past 10 and 100 Myr using the star particle ages, with,

$$\Sigma_{SFR}^{\Delta t} = \frac{M_\star(\mathrm{age} < \Delta t)}{\eta l^2 \Delta t}\ , \tag{2}$$

where $M_\star$(age $< \Delta t$) is the summed mass of all star particles in the pixel with ages less than the averaging window Δt, l^2 is the pixel size (in kpc^2), and η is a factor correcting for mass-loss from stellar winds and evolutionary effects using predictions from STARBURST99 (Leitherer et al. 1999), with values of 0.85 and 0.70 for the Δt =10 and 100 Myr time-scales, respectively. The 10 and 100 Myr intervals were chosen for their approximate correspondence with the time-scales traced by recombinations lines like Hα, and emission in the UV or FIR (Kennicutt & Evans 2012).[4] The instantaneous SFR of the gas is also considered.

We calculate column densities and mass-averaged line-of-sight velocity dispersions σ_z for (1) the total neutral gas column Σ_{gas} and (2) the 'cold and dense' gas $\Sigma_{C\&D}$ with $T < 500$ K and $n_H > 1$ cm^{-3}. The latter gas reservoir taken as a proxy for the cold molecular gas in the simulations following the methodology of Orr et al. (2018) but with a more liberal higher temperature cut for what constitutes 'cold' in the ISM. These roughly correspond to the observed velocity dispersions in the HI + H$_2$ or H$_2$ gas, respectively. We calculate the local gas velocity dispersion in each pixel as the mass-weighted standard deviation of the line-of-sight velocities of the qualifying gas elements (for each type of velocity dispersion). This is identical to taking the width of a (maximum likelihood) fitted single-component Gaussian.

We also estimate the angular velocity Ω in each pixel, defined here as

$$\Omega = \frac{v_c}{R} = \frac{(GM(<R))^{1/2}}{R^{3/2}}\ , \tag{3}$$

where R is the galactocentric radius of the pixel, and M (< R) is the total mass enclosed within a sphere of that radius.

We compare our simulations with various observational studies of spatially resolved gas line-of-sight velocity dispersions in

[3]In our analysis we treat pixels from all simulations and all times equally, unless otherwise stated.
[4]Post-processing the snapshots to explicitly model Hα or UV fluxes would make for a more direct comparison to observations, but accounting for, e.g. dust and other complexities is beyond the scope of this work, where we wish to focus on the 'true' SFRs.

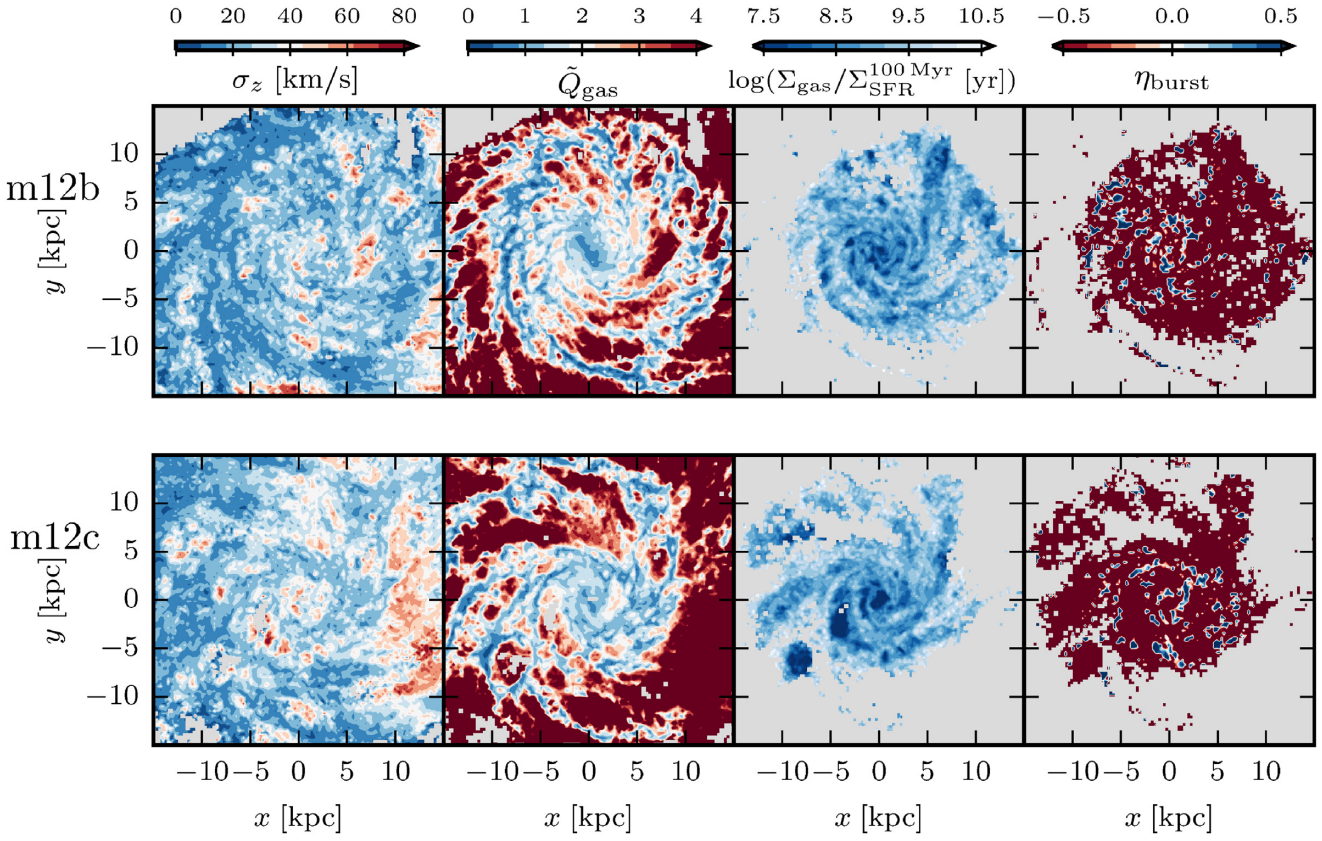

Figure 1. Face-on maps of star formation and gas quantities in two of the FIRE galaxies (rows: m12b and m12c, see Fig. A1 for other galaxy simulations) at $z = 0$ with 250 pc pixel size. Regions with fewer than ∼10 gas elements (or no star formation, in the cases of the right two columns) are excluded and coloured light grey. Left: Velocity dispersions (including inflow/outflow) in neutral (atomic + molecular) gas. Spiral structures correspond to low $\sigma_z \lesssim 40\,{\rm km\,s^{-1}}$ dispersions, with interspersed high-dispersion structures. Centre left: Turbulent Toomre-Q parameter for gas, $\tilde{Q}_{\rm gas}$. Bluer regions ($\tilde{Q}_{\rm gas} < 2$) are at least marginally unstable. Centre right: Gas depletion time averaged over 100 Myr. Several large (∼kpc) regions with short depletion times correspond with large bubbles of high-$\tilde{Q}_{\rm gas}$, indicative of SNe superbubbles. Right: 'Burstiness' measures $\eta_{\rm burst} \equiv (\Sigma_{\rm SFR}^{10\,\rm Myr} - \Sigma_{\rm SFR}^{100\,\rm Myr})/(\Sigma_{\rm SFR}^{10\,\rm Myr} + \Sigma_{\rm SFR}^{100\,\rm Myr})$. Redder (bluer) regions indicate rapidly decaying (rising) SFRs. Much of the area of the galaxies are covered by regions with decaying local star formation, while small regions with locally rising SFRs correspond to GMCs.

star-forming galaxies. Zhou et al. (2017) provide a data set at ∼kpc scales from the SAMI Galaxy Survey (Croom et al. 2012; Scott et al. 2018), relating H II region velocity dispersions to Hα-inferred SFRs. We compare these data to our neutral gas velocity dispersion and 10-Myr-averaged SFR tracers in 750 pc pixels. With our higher-resolution pixel at 250 pc, we take data from Rozas et al. (2007, H II region velocity dispersions) for comparison with neutral gas velocity dispersions in FIRE, and from Querejeta et al. (2019, HCN-traced gas velocity dispersions and dense gas depletion times) for comparison with our cold and dense gas.

3 SPATIALLY RESOLVED VELOCITY STRUCTURE AND SFRS: COMPARING SIMULATIONS AND OBSERVATIONS

Fig. 1 shows the $z = 0$ snapshots of two of the seven **m12** galaxies (by row), for a number of resolved physical quantities (by column) at a pixel size of 250 pc (the other five are found in Fig. A1 of Appendix A). Broadly speaking, the typical values of the velocity dispersions and SFRs seen in the FIRE Milky Way-mass spirals agree well with similar resolved observations of local disc galaxies (Rozas et al. 2007; Zhou et al. 2017; Querejeta et al. 2019). Across all seven of our **m12** galaxies, 95 per cent of the pixels (that also have had recent star formation according to either the 10 or 100 Myr average SFR tracer) have velocity dispersions in the neutral gas of 10–50 km s^{-1}.

The galaxies are dominated by regions with low (<40 km s^{-1}, blue shades, first column) velocity dispersions, with pockets of high-dispersion gas. Although correlated by definition, it is not easy to see structures traced by the low or high values of Toomre-Q in velocity dispersions. However, it *is* easily seen in several cases that regions with the shortest depletion times (as calculated with the 100 Myr SFR tracer, third column) do correspond to regions of high Toomre-Q. Lastly (fourth column), a measure of the 'burstiness' of star formation $\eta_{\rm burst} = (\Sigma_{\rm SFR}^{10\,\rm Myr} - \Sigma_{\rm SFR}^{100\,\rm Myr})/(\Sigma_{\rm SFR}^{10\,\rm Myr} + \Sigma_{\rm SFR}^{100\,\rm Myr})$, shows that the galaxies are dominated in area by regions that have formed stars in the past 100 Myr (and thus, for the most part, those stars have injected all their feedback already) but have had little or no star formation in the past 10 Myr. Given the small size of the regions with significant 10 Myr SFRs, this result is somewhat smoothed on 750 pc scales. The fact that the 10 and 100 Myr average SFRs are rarely equal, when considering 250 pc scales in galaxies, points to the fact that even in galaxies with consistent *global* SFRs, star formation remains quite bursty locally. Germane to this last point, recent work by Benincasa et al. (2019) has quantified that the GMC lifetimes in three of these simulations are $\lesssim 10$ Myr at $z \approx 0$, putting

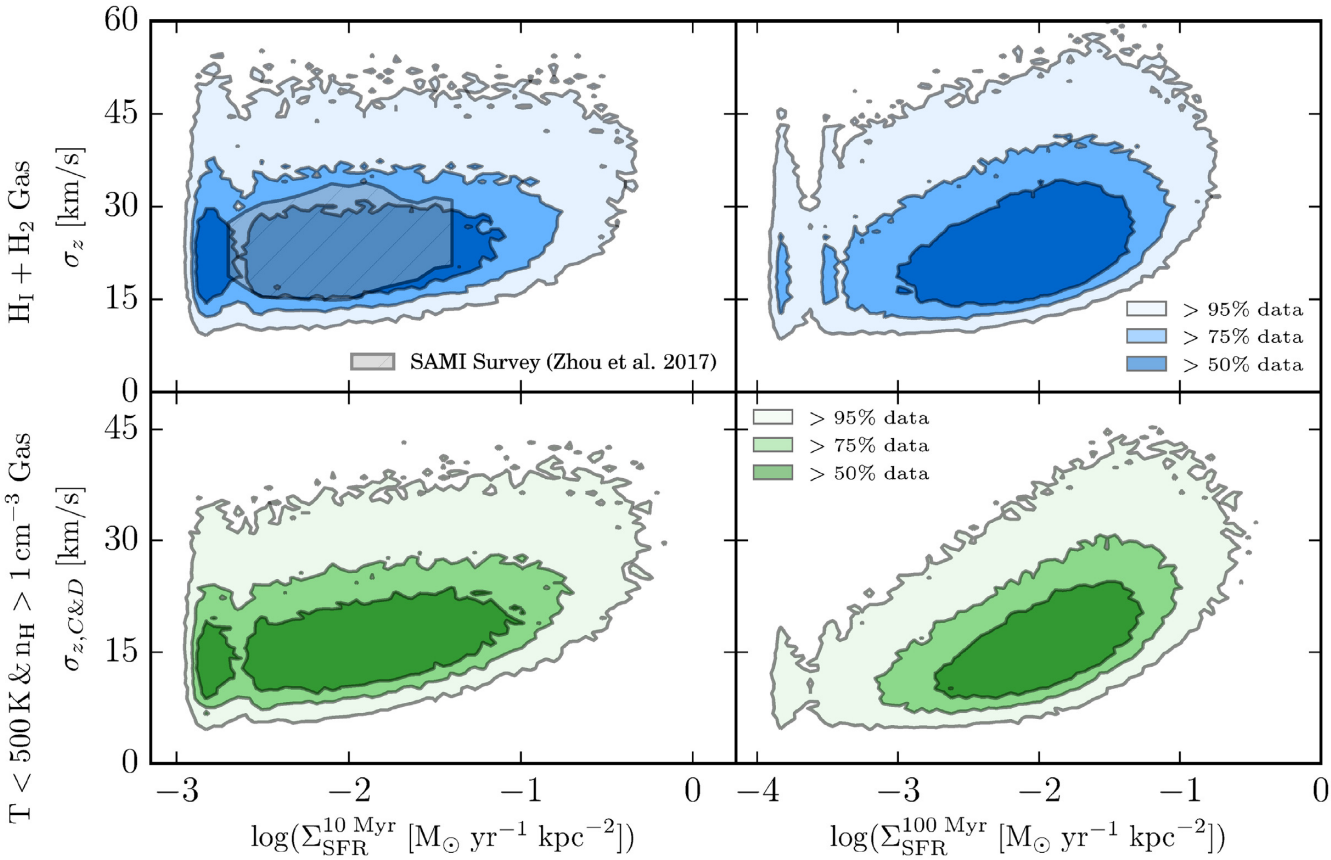

Figure 2. Distributions of spatially resolved (750 pc pixel size) line-of-sight gas velocity dispersions (σ_z) and SFR surface densities for various gas and SFR tracers in the Milky Way-mass FIRE simulations for $z \lesssim 0.1$. Gas velocity dispersions are the mass-weighted standard deviation of the line-of-sight velocities in gas, intentionally including inflow, outflow, non-circular galactic motions, etc. Data are stacked together from all individual m12 galaxy simulations (see Fig. A2). Filled contours indicate 95, 70, and 50 percentile inclusion regions for the simulation data. Velocity dispersions in neutral gas as a function of 10-Myr-averaged SFR are compared with observational data from Zhou et al. (2017). Across ∼3 dex in SFRs, gas velocity dispersions are nearly constant, with a rising lower envelope of dispersions at a given SFR. The velocity dispersions for the cold and dense gas ($T < 500$ K and $n > 1$ cm^{-3}, bottom row) are lower than for neutral gas (atomic + molecular hydrogen, top row), indicating the dynamically colder state of the dense molecular component of the ISM. Tracers with longer averaging time-scales (100 Myr versus 10 Myr, right and left columns, respectively) are able to trace the relation to lower star formation rates and gas velocity dispersions, showing that there is a trend, but that it is very weak and only apparent over longer averaging time-scales.

upper limits on the duration of any given star formation event within a GMC complex.

3.1 Various tracers of velocity dispersion and SFR time-scale

Fig. 2 shows the stacked data from all the snapshots of the Milky Way-massed FIRE spirals. We can see the velocity dispersion–SFR relation in the simulations for variously weighted tracers of gas velocity dispersion and SFR (see Fig. A2 in Appendix A for individual galaxy σ_z–SFR distributions). The extent of the data to low SFRs in each panel is mass resolution-limited, with lower limits of $\Sigma_{SFR} \approx 10^{-2.8}$, $10^{-3.75}$ $M_\odot$ yr^{-1} kpc^{-2} for the (750 pc)^2 pixels, with minimum baryonic masses of 7100 $M_\odot$ at 10 and 100 Myr (with their associated evolutionally mass correction factors), respectively.

Generally, the core of the distributions for the neutral (atomic + molecular) gas and the cold and dense gas velocity dispersions are between 15-40 km s^{-1} and 10–30 km s^{-1}, respectively. There is a tail in the distributions to ≈60 km s^{-1} and ≈45 km s^{-1} for the 95 per cent data inclusion regions for their respective ISM components. For the Milky Way-like rotational velocities $v_c \approx$ 240 km s^{-1} of these simulations, the dispersion ratios are $\sigma_z/v_c \approx$ 0.06–0.25 and 0.04–0.19 in the gas (respective to ∼ 95 per cent of the two ISM components). That is to say, the discs are thin in the FIRE **m12** simulations (see Sanderson et al. 2020 for a detailed analysis of the stellar and gas disc properties of **m12i**, **m12f**, and **m12m**).

We compare directly with the SAMI IFU data of Zhou et al. (2017) in the top left panel of Fig. 2, for our 10-Myr-averaged SFR and neutral gas velocity dispersion data. Their data has complete overlap with our 75 per cent inclusion region (and nearly total overlap with our 50 per cent region). Our inclusion of **m12w**, with its fairly 'hot' disc is a large part of the spray to higher velocity dispersions in the FIRE data. Additionally, as we orient our galaxies face-on, and thus have negligible beam-smearing or inclination effects in the line-of-sight velocity dispersions, we do not need to throw out pixels with velocity gradients as done in Zhou et al. (2017). Any velocity gradients within the face-on pixels thus correspond to disc structural properties, and warrant inclusion in our analysis.

The distributions all have increasing velocity dispersions as a function of SFRs. However, the effect is fairly weak, on the order of only a few km s^{-1} with the 10 My SFR tracer. The most visible case, with the 100 Myr SFR tracer, amounts to ∼7 km s^{-1} per dex in Σ_{SFR}, effectively doubling the velocity dispersions across our

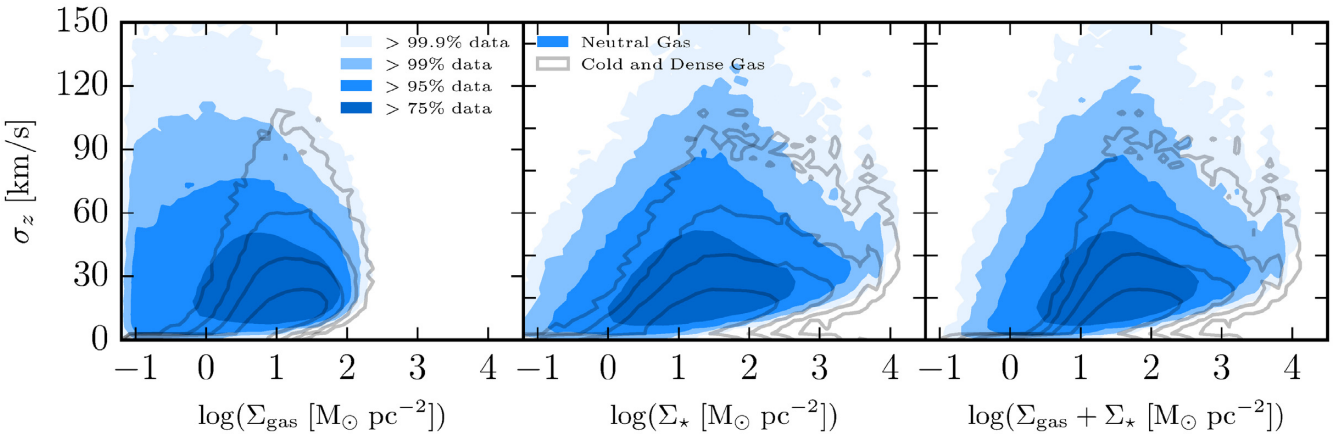

Figure 3. Distribution of σ_z (as Fig. 2) versus gas surface density ($\Sigma_{\rm gas}$), stellar surface density ($\Sigma_\star$), and total surface density ($\Sigma_{\rm gas}+\Sigma_\star$). Unfilled contours indicate velocity dispersions and gas surface densities of the cold and dense ($T<500$ K and $n>1$ cm^{-3}) component, with identical data inclusion percentages. We do not plot below $\Sigma_{\rm gas}=0.1$ M$_\odot$ pc^{-2} to ensure at least ∼10 gas elements per pixel for calculating σ_z. Left: As neutral gas surface densities exceed ∼few M$_\odot$ pc^{-2}, the ISM transitions to a predominantly molecular form, and velocity dispersions rise in the cold ISM component. Centre: Largest scatter in velocity dispersions occurs for log $\Sigma_\star\sim1.5$. Right: Total surface density–velocity dispersion distribution is very similar to the stellar surface density–velocity distribution in neutral gas, but for cold and dense gas there is a steeper rise in dispersions (and generally cold gas content) around total surface densities of ∼10 M$_\odot$ pc^{-2}. Generally higher neutral gas surface densities have a lower scatter to high dispersions, whereas the cold and dense gas velocity dispersions consistently rise with increasing gas and stellar surface densities.

dynamic range of SFRs. Universal, however, is the rising lower envelope of velocity dispersions as a function of SFR. The nature of this lower envelope is explored in Section 3.6.

3.2 Correlations with various mass surface densities

Fig. 3 shows how the line-of-sight velocity dispersions relate to the various (gas, stellar, gas + stellar) mass surface densities in the galaxies. The neutral (atomic + molecular) velocity dispersions are plotted in (blue) shaded contours, and the 'cold and dense' gas velocity dispersions are plotted in unfilled, grey contours. Generally, the neutral gas velocity dispersions exhibit less scatter at higher gas surface densities. This lessened scatter may be explained by the fact that high surface density gas discs are more self-bound gravitationally, resulting in shorter gas scale heights and thus shorter eddy turnover times for a given σ_z. If supersonic turbulence typically runs down on a eddy turnover time, then high-velocity dispersions would be quickly dissipated in the ISM. For surface densities including the stellar component (centre and right panels), the velocity dispersions peak in the range of $\Sigma_\star=10$–10^2 M$_\odot$ pc^{-2}. This peak may be an inflection point between velocity dispersions driving large-scale heights and the self-gravity of the discs increasing the rate of turbulence dissipation in the ISM.

Like the velocity dispersion–SFR relations in Fig. 2, the velocity dispersions have a lower envelope of dispersions for a given surface density. This lower limit can be rationalized as a stability limit. For dispersions below a certain value, the ISM would be gravitationally unstable to fragmentation and collapse. In this case, that unstable ISM turns into stars, both removing that gas from the dispersion relation and also causing feedback that will drive turbulence in the remaining at-least-marginally stable gas.

For all mass surface densities, the 'cold and dense' gas velocity dispersions generally rise with surface density, though always have a lower overall normalization compared to the neutral gas velocity dispersions. The rising cold and dense gas dispersions are in line with the fact that the mass fraction of that gas phase is rising, and that it is a dynamically colder component of the ISM. The rapid increase in velocity dispersions in the cold and dense gas between $\Sigma_{\rm gas}\approx1$–10 M$_\odot$ pc^{-2} overlaps with the HI to H$_2$ transition threshold generally discussed in the literature (Krumholz, McKee & Tumlinson 2008; Sternberg et al. 2014; Pineda et al. 2017).

3.3 Gas fractions, dense gas fractions, and gas stability

Fig. 4 shows the σ_z–SFR relation coloured by average pixel gas and star formation properties. The top left panel is coloured by the mass fraction of cold and dense gas in the neutral (atomic + molecular) ISM. This fraction is a rough proxy for the molecular gas fraction on ∼kpc scales. Here we clearly see that for a given amount of turbulence (velocity dispersion) more molecularly rich gas has higher SFRs on average. It is not surprising that higher dense gas fractions correspond with higher SFRs, considering that star formation occurs pre-dominantly in cold and dense gas in molecular clouds.

However, this correlation between high dense gas fractions and SFRs may appear as a bias in the observations towards higher SFRs at constant σ in the σ–$\Sigma_{\rm SFR}$ plane, when correlating SFRs with velocity dispersions that are pegged dense gas regions alone (e.g. those traced by CO $J=1\rightarrow0$ or higher transition emission). Given the difficulty/expense in measuring atomic gas (HI) on small ($\lesssim$ 100 pc) scales, a full accounting of the turbulent momentum in both the atomic and molecular ISM on kpc scales may not necessarily be done, tending towards over-weighting the dynamics of the densest gas, resulting in a 'steep' σ_z–SFR relation.

The top right panel shows the overall gas fraction, $f_{\rm gas}=\Sigma_{\rm gas}/(\Sigma_{\rm gas}+\Sigma_\star)$, another factor that clearly affects the normalization of the velocity dispersion for a given SFR. We see there is little variation in average gas fractions for a given amount of turbulence (velocity dispersion). Instead, at a given SFR, lower gas fractions yield larger turbulent velocity dispersions across 3 dex in SFRs. At lower gas fractions, for a given amount of gas (presumably, here SFRs still correlate with gas surface densities as seen before in the FIRE-1 simulations by Orr et al. 2018), a larger stellar component in the disc produces a deeper potential well for the gas to stabilize

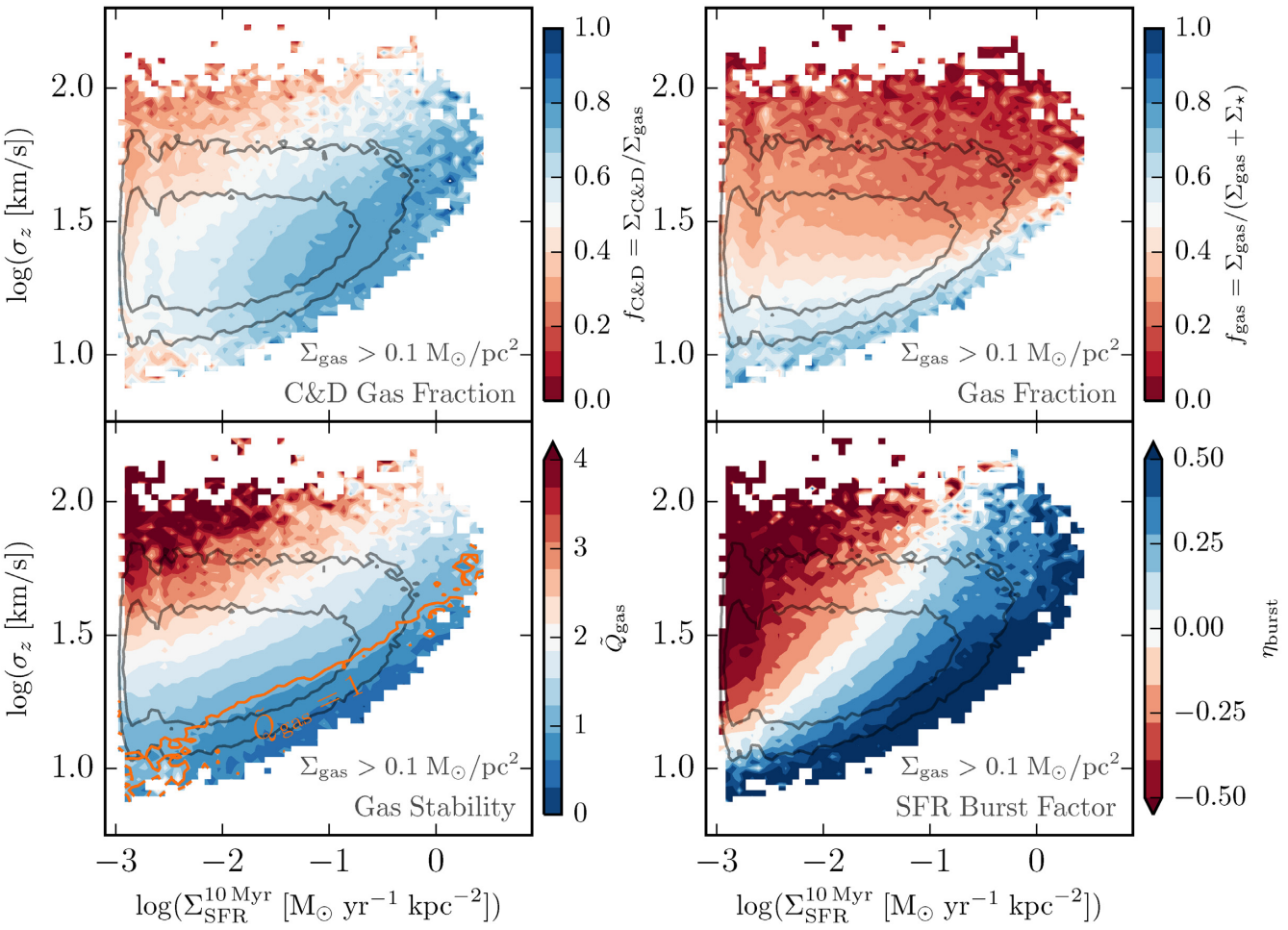

Figure 4. Distribution of σ_z and SFR (as Fig. 2, grey contours show 75 and 95 per cent data inclusion regions) coloured by various gas and star formation properties on 750 pc scales. Top left: Cold and dense gas fraction ($f_{\rm C\&D} = \Sigma_{\rm C\&D}/\Sigma_{\rm gas}$ in pixels). C&D gas fraction rises as SFR increases at constant velocity dispersion. Top right: Gas fraction ($f_{\rm gas} = \Sigma_{\rm gas}/(\Sigma_{\rm gas} + \Sigma_\star)$ in pixels). As $\Sigma_{\rm SFR}$ scales with $\Sigma_{\rm gas}$, at fixed $\Sigma_{\rm SFR}$ lower $f_{\rm gas}$ is driven by higher $\Sigma_\star$ and $\Sigma_{\rm tot}$. Gas-rich regions have the lowest velocity dispersions for their SFRs. For a constant amount of gas/star formation, gas in a deeper potential (higher stellar surface densities) must have larger velocity dispersions to maintain stability/equilibrium. Bottom left: Turbulent Toomre-Q parameter $\tilde{Q}_{\rm gas}$ (equation 1). Orange line denotes $\tilde{Q}_{\rm gas} = 1$ threshold for instabilities (i.e. pixels in this region of $\Sigma_{\rm SFR}^{10\,{\rm Myr}} - \sigma_z$ space are on-average unstable). Less stable gas (at fixed σ_z) produces higher 10 Myr average star formation rates. Bottom right: Star formation 'burstiness', $\eta_{\rm burst}$. Regions with low ratios of past to current SFRs have low σ_z at constant 10-Myr-averaged SFR, corresponding with regions of $\tilde{Q}_{\rm gas} \lesssim 1$.

itself in. Just as larger $\Sigma_{\rm gas}$ requires higher σ_z in equation (1), so does larger $\Sigma_\star$.

As neutral (atomic + molecular) gas fractions approach zero at the highest velocity dispersions ($\sigma_z > 100\ {\rm km\,s^{-1}}$), it is evident in these galaxies that an appreciable fraction of the gas is becoming ionized and is in a hot, usually outflowing state. That gas ought to no longer be considered either neutral in nature, nor in any equilibrium state (with respect to dynamics, e.g. hydrostatic/turbulent support, or related to its current SFR).

The bottom left panel of Fig. 4 shows the velocity dispersion–SFR relation coloured by the average gas stability (our modified Toomre-Q, equation 1). The average trend is similar to the trend in cold and dense gas fraction and SFRs: less stable gas is both more pre-dominantly cold and dense in nature, and has higher SFRs for a given amount of turbulence (velocity dispersion). Interestingly, the trend follows a $\sigma \propto \Sigma_{\rm SFR}^{\sim 1/6}$ relation for constant $\tilde{Q}_{\rm gas}$ (see the orange line for $\tilde{Q}_{\rm gas} = 1$, with its $\sim$1/6 slope). This power-law slope is shallower than expected for a feedback regulated, turbulent star formation environment, as derived in equation (5), suggesting that a simple turbulently regulated feedback framework alone is insufficient to describe the observed σ-$\Sigma_{\rm SFR}$ relation, and processes that raise σ at low SFR (e.g. non-negligible thermal support) and/or depress it at high SFR (e.g. momentum going into outflows or a hot ISM phase instead of neutral gas σ) are required at a minimum.

That there are patches at (albeit) low 10-Myr-averaged SFR that have such high values of $\tilde{Q}_{\rm gas} (\gtrsim 3)$ is interesting: regions with $\tilde{Q}_{\rm gas} > 1$ are expected to be stable against star formation, i.e. to have no/very little current (instantaneous) star formation. The fact that high $\tilde{Q}_{\rm gas}$ regions do have non-zero 10 Myr SFRs suggests that star-forming regions may be able to regulate and inject sufficient stabilizing feedback momentum on sub-10 Myr time-scales. Admittedly, this interpretation may be complicated if a significant number of *independent* star forming regions overlap within the 750 pc pixels. However, this time-scale corresponds to both the bulk of ionizing radiation from massive stars and the first

(few) SNe in a GMC. And indeed, Benincasa et al. (2019) found that many of these GMCs had lifetimes $\lesssim 10$ Myr.

As well, all of the velocity dispersions calculated for the neutral gas are in excess of $\sim$10 km s^{-1}, above the sound speed for 8000 K atomic gas $c_s \approx 6$ km s^{-1}. These in excess of 10 km s^{-1} velocity dispersions are in line with many observations of the star-forming ISM, where few, if any, star-forming regions are purely thermally supported even at the lowest SFR surface densities (Stilp et al. 2013a, b).

3.4 Velocity dispersions and SFR time-scales

The bottom right panel of Fig. 4 investigates correlations within the σ_z–SFR relation, when considering the 10 Myr average SFR and neutral gas σ_z, on the recent star formation history of the pixels. Here we colour the relation by the star formation burst measure $\eta_{\rm burst}$, where bluer (redder) patches indicate rising (falling) SFRs in time, corresponding with the injection of feedback over time as patches evolve from blue to red following a starburst.

Probing SFRs on 100 versus 10 Myr time-scales provides an interesting test of the feedback-regulation picture, where longer SFR tracers are sensitive to regions that have already injected all, or a significant fraction, of their feedback budget. Thus, shorter time-scale tracers are indicative of the current demands of the ISM, feedback-wise, whereas longer tracers should trace the more-averaged history of the momentum balance in the ISM. Hence, bluer patches indicate currently unstable star-forming regions (presumably with star-forming, or very recently dispersed, GMCs, Benincasa et al. 2019), while redder regions reflect those that have presumably received the bulk of feedback from young stars following a starburst. The lower envelope of the relation appears to follow a curve where a single star formation event has occurred in the last 10 Myr, such that $\Sigma_{\rm SFR}^{\rm 100\,Myr} \sim \Sigma_{\rm SFR}^{\rm 10\,Myr}/10$. And so, at low recent (10 Myr) SFRs, the amount of star formation that has occurred in the past 100 Myr is strongly correlated with the amount of turbulence (velocity dispersion) in the ISM. There is essentially space between the velocity dispersion floor and ceiling (cf. Section 3.6) for on-off star formation cycles to occur over 100 Myr time-scales. However, at high recent SFRs, both the dynamical times of the regions become shorter (thus leaving little room temporally for on-off star formation modes) and the velocity dispersions cannot be driven much higher before hitting an outflow threshold. Thus, the 100-Myr-averaged tracer at very high recent SFRs approaches $\Sigma_{\rm SFR}^{\rm 100\,Myr} \approx \Sigma_{\rm SFR}^{\rm 10\,Myr}/10$ (modulo stellar evolution mass-loss correction factors) with a single star formation event. At these high SFRs, the ISM effectively has no feedback history locally, and is in an unstable, highly star-forming state.

3.5 Depletion times in neutral and cold & dense gas

Fig. 5 explores how gas depletion times vary across the velocity dispersion–SFR relation for both 250 pc and 750 pc pixel sizes. We explore both how the depletion time of the cold and dense gas and of all neutral gas vary with their respective velocity dispersions for the 10-Myr-averaged tracer of star formation. Here we directly compare with three observational data sets: two HII velocity dispersions and Hα SFR studies (Rozas et al. 2007; Zhou et al. 2017), and one of the velocity dispersions and depletion times in HCN (tracing very cold and dense gas, Querejeta et al. 2019). Neither the Rozas et al. (2007) nor the Zhou et al. (2017) data sets include gas depletion time estimates, and so only constrain the extent of our σ–SFR relation. With these, we find good agreement.

The Querejeta et al. (2019) data, however, did include measurements of the depletion time of the dense gas. We compare our cold and dense depletion time data directly against the $\Sigma_{\rm SFR}/\Sigma_{\rm HCN}$ with the same colourbar, and find very good agreement. Particularly interesting for comparison with the Querejeta et al. (2019) data, there are two distinct (bluer) regions with shorter dense gas depletion times on 250 pc scales: (1) low velocity dispersions for a given 10-Myr-averaged SFR, which is the scaling that their observational data set covers and (2) high 10-Myr-averaged SFRs *and* high $\gtrsim 30$ km s^{-1} dense gas velocity dispersions, which their data set did not trace. At 750 pc pixel size, the short depletion time region at low velocity dispersions is not seen as strongly, with $\tau_{\rm dep} = \Sigma_{\rm gas}/\Sigma_{\rm SFR}$ falling to $\sim 10^{8.5}$ yr at low velocity dispersions.

Interpreting further the case where dense gas depletion times become short at low $\sigma_{z,\rm C\&D}$, this appears to happen in pixels in the simulations where only a small fraction of the ISM is cold and dense (and its contribution to the overall turbulent momentum is low). This case occurs in galactic outskirts where the ISM is considerably more diffuse, but requires some stabilizing feedback. There, the ISM evolves to produce just enough dense gas to form stars, but in the process is rapidly consumed.

3.6 Outflow-prone gas fractions: balancing self-gravity and integrated feedback

Fig. 6 explores the role of an outflow threshold in setting the limits of the turbulence in the ISM for a given SFR and recent star formation history. In previous sections, we explored how the velocity dispersion–SFR relation depends on properties of the gas and, to an extent, recent star formation. However, the 'edges' in the relation are correlated seemingly with the (neutral) gas fractions (high- and low-σ_z limit) and gas stability ($\tilde{Q}_{\rm gas}$, lower σ_z limit at constant SFR). Naturally, regions that approach having no neutral gas ($f_{\rm gas} \rightarrow 0$) will no longer be able to support star formation. As well, patches of the galaxy can only be so unstable ($\tilde{Q}_{\rm gas} \rightarrow 0$). The third edge in the relation here, that of a minimum SFR, is resolution limited in these simulations, and not indicative of a physical cut-off in SFRs. However, there was not a clear reason physically for either the $f_{\rm gas} \rightarrow 0$ or the $\tilde{Q}_g \rightarrow 0$ edge to occur where they did, in terms of the normalization of σ_z.

Rescaling the velocity dispersions by their ratios to the local circular velocity in the galaxy, as is often discussed when considering galactic outflows, we see first that the vast majority (>75 per cent by area) of the galaxies have disc aspect ratios v_c/σ_z between $\sim 4-20$. The simulations have, by and large, thin discs over most of their areas.

We consider an outflows-threshold from of Hayward & Hopkins (2017), where there is a surface density threshold in the gas for which a given amount of feedback per area in time $(P/m_\star)\Sigma_{\rm SFR}$ can accelerate that patch of gas to the local escape velocity in a coherence time (roughly equivalent to an eddy crossing time). This threshold, equation (5) in Hayward & Hopkins (2017), is $\Sigma_{\rm gas} < (P/m_\star)\Sigma_{\rm SFR}/\sqrt{2}R\Omega^2$. In Fig. 6, we shade the (σ_z/v_c)–$\Sigma_{\rm SFR}$ relation by the fraction of pixels that have gas surface densities below this threshold and thus find themselves 'outflow-prone' at that position in (σ_z/v_c)–$\Sigma_{\rm SFR}$ space. Interestingly, the different edges of the (σ_z/v_c)–$\Sigma_{\rm SFR}$ relation for neutral gas velocity dispersions and the 10 Myr SFR tracer, excluding the mass resolution limit, map to the regimes where significant fractions of gas become outflow-prone depending on the different time-scale star formation tracers. As the local coherence time is of the order of the eddy crossing time,

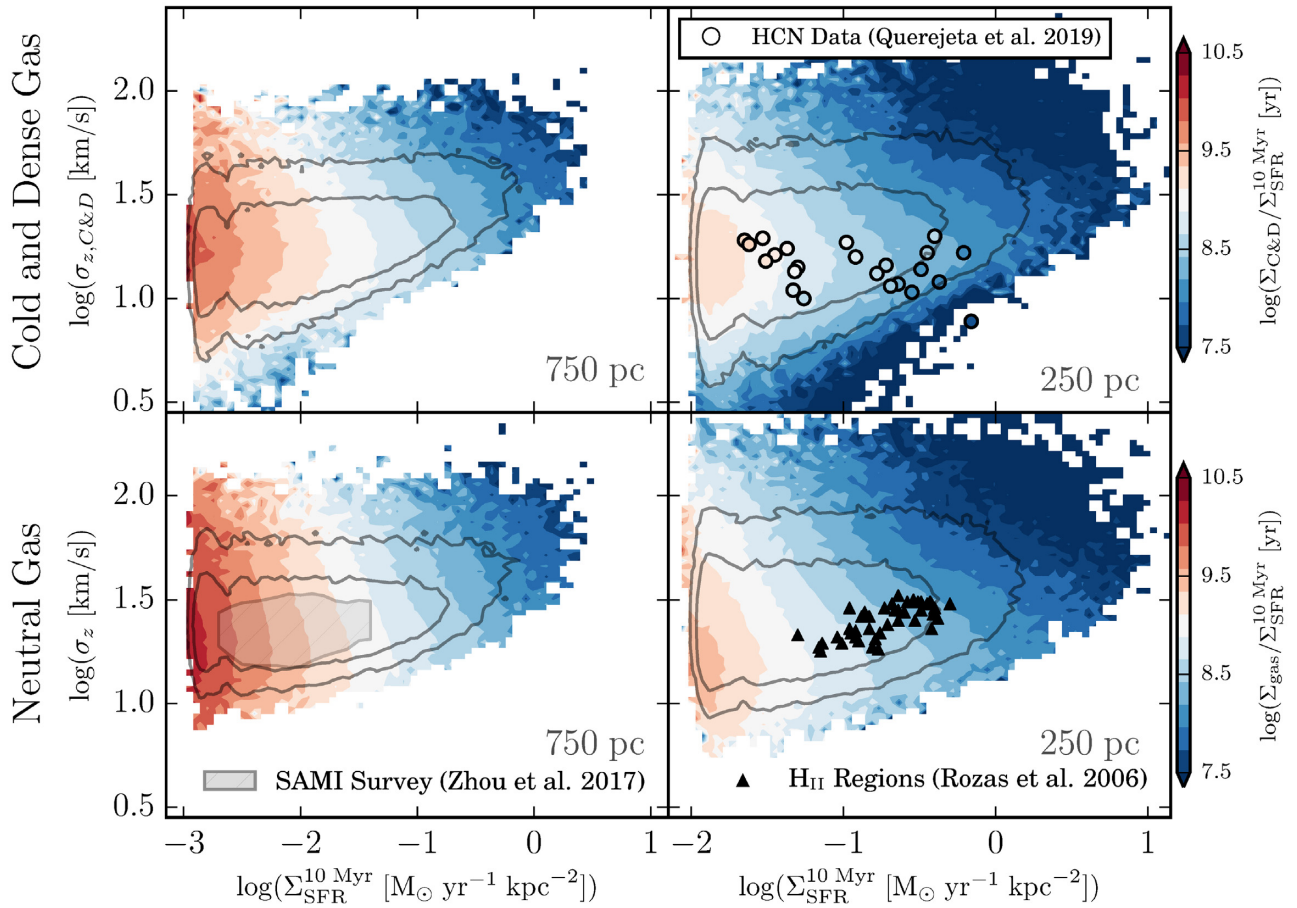

Figure 5. We compare σ_z (as Fig. 2) in cold and dense gas (top row) or all neutral gas (bottom row) with 750 pc (left column) or 250 pc (right column) pixels, coloured by the gas depletion time, to corresponding observations *also coloured* (where possible) by depletion time. Dispersions (σ_z) are only weakly correlated with depletion time at fixed $\Sigma_{\rm SFR}$, as observed. Cold and dense gas exhibits two regimes of short depletion times, gas with high σ_z and SFRs, and with low σ_z at fixed SFR tending towards short (∼few 10^7 yr) dense gas depletion times. The core of the simulation data distributions and observations agree well. Higher scatter to large velocity dispersions in the simulation data may be attributable to observational selection effects, e.g. comparing cold and dense gas in the simulations with *very cold and very dense* gas tracers like HCN.

all of the star formation tracer time-scales explored are roughly equivalent or shorter than ∼100 Myr, so each tracer integrates parts of the feedback that end up driving outflows (i.e. the instantaneous tracer only tracing radiative pressure and winds, whereas the 10-Myr-averaged tracer integrates both those and early Type-II SNe).

Focusing on the material that is outflow-prone when considering the instantaneous SFR, it appears that the hard-limit in the velocity dispersion-SFR relation at constant σ is set by the amount of momentum that the ISM can absorb before appreciable fractions of it are blown out efficiently. On short (<10 Myr) time-scales, as per the discussion in Section 4.1, it is reasonable to consider σ constant or only very slowly varying as star formation *fires* up. On the other extreme of our star formation tracer time-scales, when we consider the outflow fractions as calculated by the 100 Myr tracer, we see that the outflow-prone material traces the most extreme σ_z/v_c, above $\log(\sigma_z/v_c) \geq -0.5$. That this gas has the highest amount of dispersion support ($\propto \sigma_z/v_c$) is understandable, as on 100 Myr time-scales, feedback is able to pump velocity dispersions on disc scales, and regions that are marginally outflow-prone and still have any gas left will have the highest velocity dispersions. After all, these kpc-patches have absorbed the full feedback from one or more young star clusters. The outflow fraction approaching unity for 100 Myr time-scale SFRs in disc environments thus provides a physical reason for the top edge of the (σ_z/v_c)-$\Sigma_{\rm SFR}$ relation.

The 10 Myr SFR tracer prediction, lying between these two natural extreme time-scales, connects the two limits, representing regions that are seemingly either maximally forming stars locally (and regulated by prompt feedback like radiation pressure and stellar winds), or have velocity dispersions approaching escape velocity, presumably due to recently injected feedback.

3.7 Gas properties correlating with gas stability budgets: does the degree of turbulence matter?

Fig. 7 plots the predicted velocity dispersions in each pixel, assuming $\tilde{Q}_{\rm gas} = 1$ versus the measured σ_z, and colours the relation by average gas fractions, outflow-prone fractions (calculated with the 100 Myr tracer) and $\eta_{\rm burst} = (\Sigma_{\rm SFR}^{10\,\rm Myr} - \Sigma_{\rm SFR}^{100\,\rm Myr})/(\Sigma_{\rm SFR}^{10\,\rm Myr} + \Sigma_{\rm SFR}^{100\,\rm Myr})$, a measure of the star formation burstiness. If all the patches of the galaxies had $\tilde{Q}_{\rm gas} = 1$, then the whole data set would fall on the dotted $\tilde{Q}_{\rm gas} = 1$ line, so the plots show how these quantities vary with how far from equilibrium individual regions are. The floor in σ_z appears where the atomic phase of the ISM (stable at $T \approx 6000$ K) provides non-negligible thermal support with

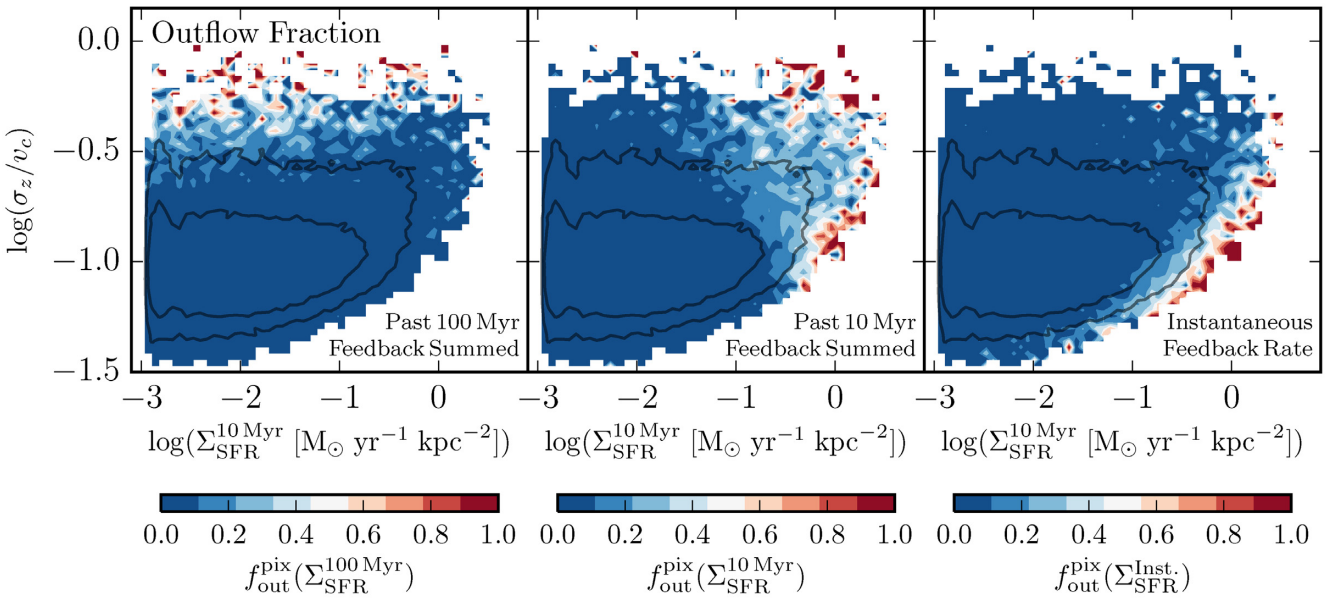

Figure 6. Distribution of $\Sigma_{\rm SFR}^{\rm 10\,Myr}$ versus σ_z relative to the local circular velocity $v_{\rm c}$ (style as Fig. 4), now coloured by the theoretical prediction for whether the gas $f_{\rm out}$ should be unbound by feedback in 'steady state' (see Section 3.6 in the text) from the model in Hayward & Hopkins (2017) (given $\Sigma_{\rm SFR}$, $v_{\rm c}$, and R). Colouring is by the average fraction of pixels whose gas meets the outflow criterion at that point in $\Sigma_{\rm SFR}$–$\sigma_z/v_{\rm c}$ space. If we calculate $f_{\rm out}$ from the SFR averaged on 100 Myr time-scales (left panel), i.e. $\sim t_{\rm dyn}$ of the galaxy it neatly matches where gas is outflowing ($\sigma_z \gtrsim v_{\rm c}$); but if we calculate $f_{\rm out}$ using the 'instantaneous' SFR (right panel), it corresponds not to where present outflows exist (the outflows have not developed), but it defines the 'upper limit' of $\Sigma_{\rm SFR}$, where local 'early' feedback shuts down dense gas collapse. Averaging over 10 Myr time-scales (middle panel), there is an intermediate scenario, where outflows are developing and gas is being driven to high σ_z approaching local escape velocities.

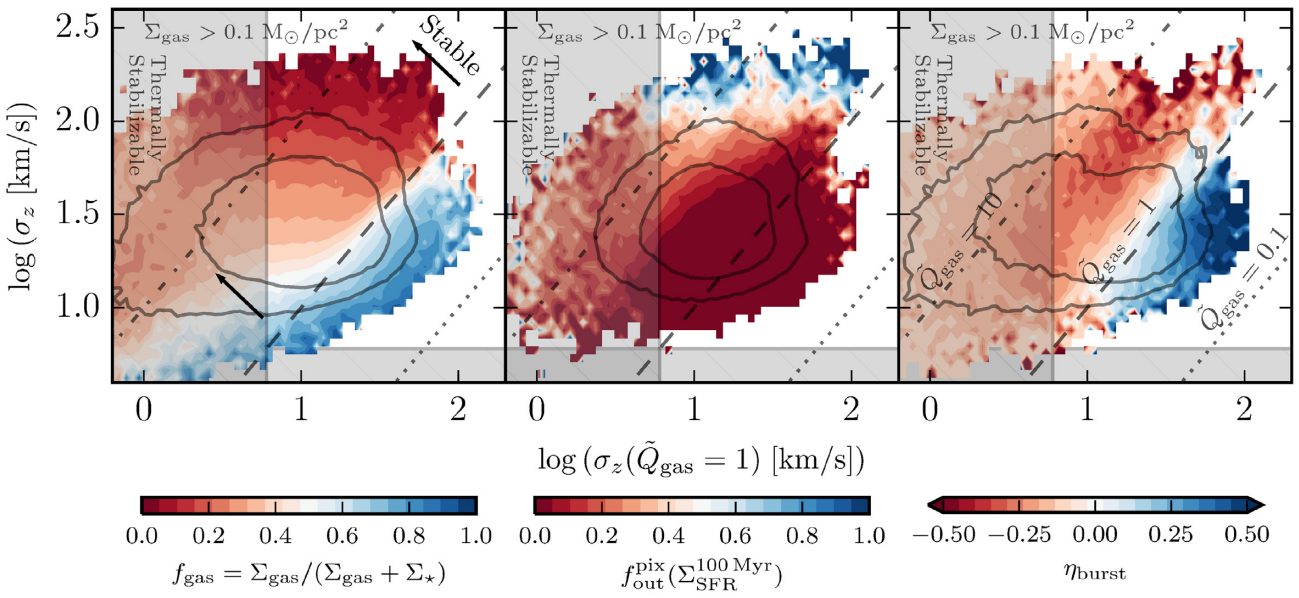

Figure 7. Distributions of gas velocity dispersion required for a given pixel (750 pc) to have $\tilde{Q}_{\rm gas} = 1$ (equation 1), versus actual σ_z in neutral gas, coloured by average pixel gas fraction (*left*), whether the 100 Myr SFR predicts outflows (middle), or star formation 'burstiness' $\eta_{\rm burst}$ (right). Considering regions with $\sigma_z(\tilde{Q}_{\rm gas} = 1) > 6$ km s^{-1} (i.e. regions that *cannot* be only thermally supported), gas rich regions ($f_{\rm gas} \rightarrow 1$) are unstable to gravitational collapse and fragmentation ($\tilde{Q}_{\rm gas} < 1$), whereas the most gas poor regions ($f_{\rm gas} \rightarrow 0$) have high velocity dispersions and lie in the $1 < \tilde{Q}_{\rm gas} \lesssim 10$ regime. Similarly, high σ_z is a stronger predictor of whether or not a region is likely to host outflows ($f_{\rm out}^{\rm pix} \rightarrow 1$) than $\tilde{Q}_{\rm gas}$, provided $\tilde{Q}_{\rm gas} > 1$. Interestingly, for regions that *can* be thermally stabilized, the fraction of regions capable of hosting outflows rises strongly with $\tilde{Q}_{\rm gas} \gtrsim 3$. Regions with rapidly rising (decaying) local SFRs correspond to regions with $\tilde{Q}_{\rm gas} < 1$ ($\tilde{Q}_{\rm gas} > 1$).

$c_{\rm s} \approx 6$ km s^{-1}. The required σ_z to stabilize the gas (for $\tilde{Q}_{\rm gas} = 1$) can fall to arbitrarily low values, and any amount of thermal support may be sufficient to maintain stability (also represented by a greyed-out patch for $\sigma_z(\tilde{Q}_{\rm gas} = 1) < 6$ km s^{-1}).

Concerning local gas fractions $f_{\rm gas}$ in the simulations, regions with $\tilde{Q}_{\rm gas} < 1$ are on-average gas rich with $f_{\rm gas} > 0.5$. The most stable regions requiring turbulent support $\sigma_z(\tilde{Q}_{\rm gas} = 1) > c_s \approx 6$ km s^{-1} are the least gas rich, with higher values of σ_z having $f_{\rm gas} \rightarrow 0$.

The middle panel shows the outflow-prone fraction calculated using the 100 Myr average SFR. High-velocity dispersion, low gas fraction regions are the only areas with significant outflow-prone fractions. This suggests that significant feedback events over 100 Myr time-scales have had a chance to drive these dispersions to high values, i.e. $\tilde{Q}_{\rm gas} \gg 1$. Evidently, these regions do not just have high-velocity dispersions because they have deep disc potentials with high $\Sigma_\star$, though these are correlated to an extent.

Finally, looking at an indicator of how bursty star formation is, i.e. the relative amount of star formation occurring now versus in the recent past, $\eta_{\rm burst}$, we see that the $\tilde{Q}_{\rm gas} = 1$ threshold is a demarcating line between an abundance of current star formation as compared to the past (bluer shading) and vice versa. The right-hand panel of Fig. 7 shows that vigorous star formation occurs in the ISM when the gas is gravitationally unstable against fragmentation, and collapses on the Toomre-scale (here, the disc scale height).

Exploring this last aspect further, Fig. 8 shows how the gas depletion time (calculated by the time for neutral gas consumption with two different star formation tracers, the gas instantaneous and 10 Myr average SFR) correlates with gas stability using $\tilde{Q}_{\rm gas}$. The relation is shaded by the star formation burst indicator $\eta_{\rm burst}$. Importantly, we exclude gas outside 3 kpc $< R <$ 10 kpc, and with $\Sigma_{\rm gas} < 0.1$ M$_\odot$ pc^{-2}, as it is either not shielded and likely has significant thermal support, or is at radii with a rising rotation curve and has significant shear across the 750 pc pixels, such that the assumption of a flat rotation curve in calculating $\tilde{Q}_{\rm gas}$ breaks down and it is no longer a good measure of gas stability.

When considering the instantaneous SFR gas depletion time, we see that $\tilde{Q}_{\rm gas}$ alone is a good predictor of $\eta_{\rm burst}$, with less stable regions having significant current relative to past star formation. Notably, there are few regions with $\eta_{\rm burst} \lesssim -0.5$, i.e. pixels that have significant instantaneous (current) star formation and have recent star formation histories dominated by past (10 Myr $< t_{\rm ago} <$ 100 Myr) star formation.

On the other hand, the 10 Myr average SFR gas depletion time panel shows two regimes: (1) short depletion times are dominated by regions with more recent versus past star formation ($\eta_{\rm burst} >$ 0.5) and are on-average less stable ($\tilde{Q}_{\rm gas}$ is ∼0.3 dex lower), and (2) long-depletion time regions have slightly higher values of $\tilde{Q}_{\rm gas}$ on-average, and are dominated by past versus recent star formation. The on-off cycle picture is further borne out when considering the 100-Myr-averaged gas depletion times (bottom panel). The patches with the shortest depletion times averaged over 100 Myr (i.e. most integrated star formation per unit *remaining* gas) are the most stable on average. That there exist bursts of star formation agrees with recent work by Orr et al. (2019), where on-off cycles of star formation can be driven on 1/Ω time-scales by feedback from Type II SNe and their ∼40 Myr delay time distribution.

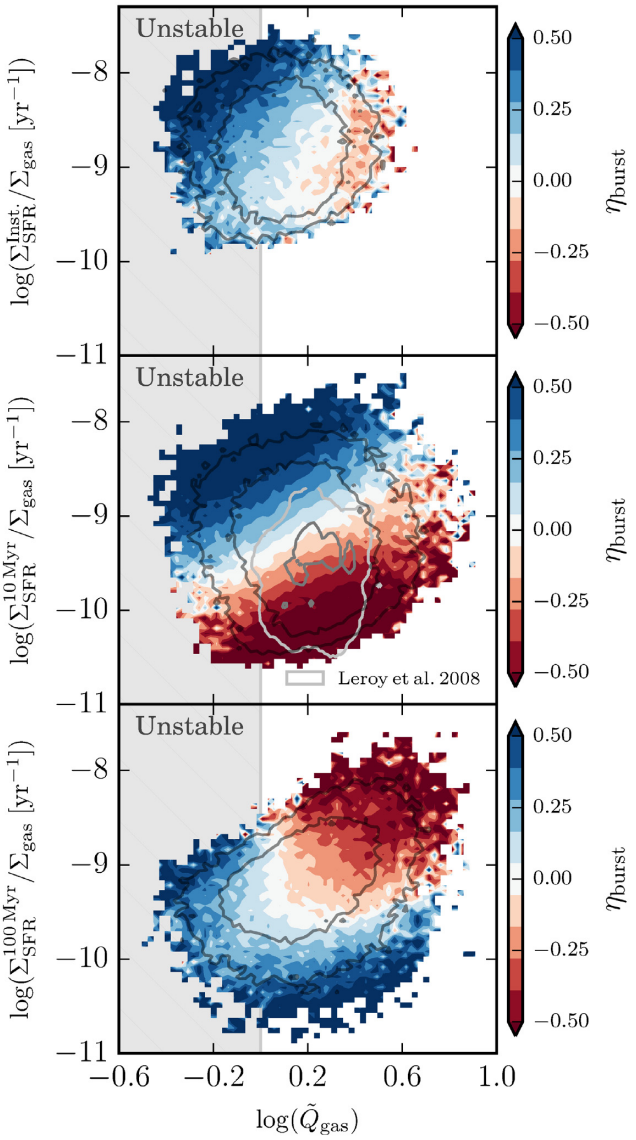

Figure 8. Distribution of pixel inverse depletion times (using SFR averaged on different time-scales), labelled versus local $\tilde{Q}_{\rm gas}$, coloured by star formation 'burstiness' parameter $\eta_{\rm burst}$ (as Fig. 1), compared where appropriate with spatially resolved observations of Leroy et al. (2008). Grey contours indicate 95 and 75 per cent data inclusion regions (by pixel number). Pixels are cut for $\Sigma_{\rm gas} < 0.1$ M$_\odot$ pc^{-2} and outside of $3 < R/{\rm kpc} < 10$. As gas clusters are very close to $\tilde{Q}_{\rm gas} = 1$, there is almost no direct correlation between $\tilde{Q}_{\rm gas}$ and (inverse) depletion time. Gas with rising (decaying) SFRs does tend towards smaller (larger) $\tilde{Q}_{\rm gas}$.

4 DISCUSSION

4.1 A hierarchy of time-scales: why is σ_z–$\Sigma_{\rm SFR}$ so flat?

It is notable that for three dex in (10-Myr-averaged) SFRs, σ_z hardly budges (cf. Fig. 2), the lower envelope in velocity dispersions notwithstanding. This flatness in velocity dispersions however, like the discussion regarding scatter in the resolved Kennicutt-Schmidt relation at high spatial resolution (Schruba et al. 2010; Kruijssen & Longmore 2014; Orr et al. 2019), may be understood through a discussion of a hierarchy of time-scales. Within the framework of supersonic turbulence dominating the velocity dispersions, the turbulent momentum in a patch of the ISM is decaying on an eddy-crossing time $t_{\rm eddy} \sim 2/\Omega$, and so $\dot{\sigma_z} \sim -2\sigma_z\Omega$. For the Milky Way-like galaxies explored here, $\Omega = v_{\rm c}/R \sim 250$ km s^{-1} /10 kpc ∼25 Gyr^{-1}; thus, $t_{\rm eddy} \sim 80$ Myr. This time-scale is far longer than the free-fall time for a GMC with a mean density of $n = 100$ cm^{-3}, $t_{\rm ff} = \sqrt{3\pi/32Gm_p n} \approx 5$ Myr (see also the simulated GMC lifetimes of Grudić et al. 2018 & Benincasa et al. 2019). As a result, while σ_z only slowly evolves as turbulence is dissipating, short time-scale tracers of star formation do not persist long enough to trace the effects of feedback as it is felt/absorbed by the ISM on the relevant scales for the gas velocity dispersions (of course, 'prompt' feedback like winds and ionizing radiation are locally felt immediately). Considering that the feedback momentum

from supernovae in a star cluster is meted out over a period of $\sim 5 - 40$ Myr (to say, $t_{\rm fb} = 40$ Myr), it is understandable that some evolution in σ_z is seen for σ-$\Sigma_{\rm SFR}$ when considering the 100-Myr-averaged SFR tracer. This longer-time-scale SFR tracer is able to overlap with the entire feedback injection period, not just the start of it. This differential-time-scales picture is especially true when considering the gas instantaneous SFR, where there is effectively no evolution in the velocity dispersions as the SFR ramps up and down per the local ISM conditions. Instantaneous SFRs do not appear to have any correlation with velocity dispersions in the ISM (barring the slight lower envelope in velocity dispersions for a given instantaneous SFR, seen more strongly for the 10 and 100 Myr SFR relations). The initial distribution of velocity dispersions is simply smeared out across the range of SFRs as they rapidly rise and fall. And so, it is expected that we see a flat distribution in velocity dispersion, and a slightly positive slope in it, for 10 Myr and 100 Myr tracers of star formation, respectively, with a hierarchy of time-scales: $t_{\rm ff} \lesssim 10\,{\rm Myr} < t_{\rm fb} < 100\,{\rm Myr} \sim t_{\rm eddy} \sim 1/\Omega$.

4.2 What drives velocity dispersions (theoretically)?

There have been a number of attempts to understand the theoretical relationship between local SFRs and the local gas disc structure (e.g. scale height, velocity dispersion). Often, these attempts have been viewed through the lens of star formation as an equilibrium process in galaxies (e.g. Ostriker & Shetty 2011; Faucher-Giguere et al. 2013; Hayward & Hopkins 2017), given the fact that the most massive stars form and live only for a fraction of a galactic dynamical time. However, some work has sought to understand how non-equilibrium models of star formation might behave in Milky Way-like disc environments, when gas dynamical and stellar feedback time-scales are on a comparable footing (Benincasa et al. 2016; Orr et al. 2019).

Generally, models of star formation in discs either invoke feedback as a regulator of either the gravitational weight of discs or the momentum in the cold turbulent ISM or posit that star formation is solely a consequence of gas dynamics in the disc. Usually, SFRs are tied in some way to the turbulence (velocity dispersion) in the gas disc. However, there are classes of models where star formation is the result of disc/galactic structure and acts as a regulator of ∼kpc-scale ISM structure and is not explicitly related to σ, for instance that of Ostriker & Shetty (2011), where the feedback from stars balances the weight of the disc. The weight of a disc being approximately described as $\frac{\pi}{2} G \Sigma_{\rm gas}(\Sigma_{\rm gas} + \gamma \Sigma_\star)$, where the γ term is the fraction of the stellar surface density within a gas scale height. This weight is balanced with the feedback momentum $(P/m_\star)\Sigma_{\rm SFR}$. Thus, $(P/m_\star)\,\Sigma_{\rm SFR} \approx \frac{\pi}{2} G \Sigma_{\rm gas}(\Sigma_{\rm gas} + \gamma \Sigma_\star)$. This formulation for the SFR is agnostic to the actual velocity dispersion or scale height of the gas disc.[5] Often, however, it *is* connected by invoking $\tilde{Q}_{\rm gas} \sim \sigma\,\Omega/\,\Sigma_{\rm disk} \sim 1$, in which case the result is identical to the scaling derived from balancing feedback-injection with turbulent dissipation. Barring that assumption, this feedback-balanced formulation actually makes *no direct* prediction of the velocity dispersions or turbulence in the disc.

Among many scalings for galactic discs, there are several which are broadly argued for to explain velocity dispersions in Milky Way-like galaxies:

(i) **Marginal gas stability ($\tilde{Q}_{\rm gas} = 1$):** Gas drives itself to marginal stability against gravitational fragmentation and collapse (per the earlier discussion in Section 1), as measured by the Toomre-Q parameter (Toomre 1964). If there is sufficient turbulent support (σ) against fragmentation, it is expected that gas would continuously dissipate turbulent energy (σ) until that gas becomes unstable and fragments, collapsing into stars. As part of a feedback-regulation framework, it would be argued that those newly formed stars would inject momentum to drive the remaining gas back to turbulent stability, hence the fragmentation threshold of $\tilde{Q}_{\rm gas} = 1$ (equation 1) representing a natural equilibrium solution, and predicting velocity dispersions to scale as

$$\sigma_{z,(Q=1)} = \frac{\pi G(\Sigma_{\rm gas} + \gamma\,\Sigma_\star)}{\sqrt{2}\Omega}\ . \tag{4}$$

(ii) **Turbulent momentum injection balances dissipation:** The rate of feedback momentum injected by massive stars balances the rate of turbulence dissipation in the supersonic ISM (e.g. Faucher-Giguere et al. 2013; Hayward & Hopkins 2017). Here, turbulent momentum is argued to decay on an eddy (disc) crossing time, where $P_{\rm turb} \sim \Sigma_{\rm gas}\sigma$ and so $\dot{P}_{\rm turb} \sim -\Sigma_{\rm gas}\sigma\Omega/2$. The turbulence dissipation is balanced with feedback injection, injected at a rate of $(P/m_\star)\Sigma_{\rm SFR}$. Together, $(P/m_\star)\Sigma_{\rm SFR} \approx \sqrt{3}\Sigma_{\rm gas}\sigma_z\Omega/2$. Or,

$$\sigma_{z,FB} \approx \frac{2}{\sqrt{3}}(P/m_\star)\frac{\Sigma_{\rm SFR}}{\Omega\,\Sigma_{\rm gas}}\ . \tag{5}$$

The intuition for this scaling is fairly straightforward: in order to maintain high levels of gas turbulence (velocity dispersion), large amounts of momentum (sourced from stellar feedback) need to be continually injected. Combined with the argument that discs regulate themselves to $\tilde{Q}_{\rm gas} \approx 1$, this model does a fairly good job matching observations of the Kennicutt-Schmidt relation (Orr et al. 2018), and so it and the previous formulation are often conflated as the 'feedback-regulated' model.

(iii) **Constant (low) efficiency star formation:** Star formation proceeds at a constant efficiency per free-fall time in a gas disc (e.g. Krumholz, Dekel & McKee 2012; Salim, Federrath & Kewley 2015). Here, $\Sigma_{\rm SFR} = \epsilon_{\rm ff}\Sigma_{\rm gas}/t_{\rm ff}$, where $\epsilon_{\rm ff} \approx 0.01$, and $t_{\rm ff}$ can be derived arguing that the self-gravity of the stellar component is important, hence: $t_{\rm ff} \approx \sqrt{3\pi\sigma_z/32G\Omega\Sigma_{\rm disk}}$. Combining this with previous statement of constant efficiency, we find that the SFR scales as $\Sigma_{\rm SFR} \propto \epsilon_{\rm ff}\Sigma_{\rm gas}\Omega^{1/2}\Sigma_{\rm disk}^{1/2}/\sigma_z^{1/2}$. And thus the velocity dispersions scale explicitly as

$$\sigma_{z,CE} \approx \frac{32G}{3\pi}\epsilon_{\rm ff}^2\frac{\Omega\Sigma_{\rm gas}^2\Sigma_{\rm disk}}{\Sigma_{\rm SFR}^2}\ . \tag{6}$$

This scaling has the opposite intuition from the feedback-regulated model: low velocity dispersion (i.e. razor-thin) discs will have very high SFRs, and high-dispersion discs will have low SFRs. There is no explicit connection to gas stability in the form of $\tilde{Q}_{\rm gas} \approx 1$.

(iv) **Accretion-powered turbulence/star formation:** The gravitational potential energy of in-falling gas is converted to turbulent motions, i.e. σ, and gas migrates through the disc to the centres of galaxies, all while star formation is occurring (Klessen & Hennebelle 2010; Krumholz & Burkert 2010; Cacciato, Dekel & Genel 2012; Krumholz et al. 2018).

Starting from the assumption that gas follows, albeit slowly decaying, circular orbits, the change in gravitational energy in time for a

[5]The gas scale height ($\sim\sigma_z/\Omega$) does indirectly enter into γ, in the relative difference in scale heights of the gaseous and stellar discs.

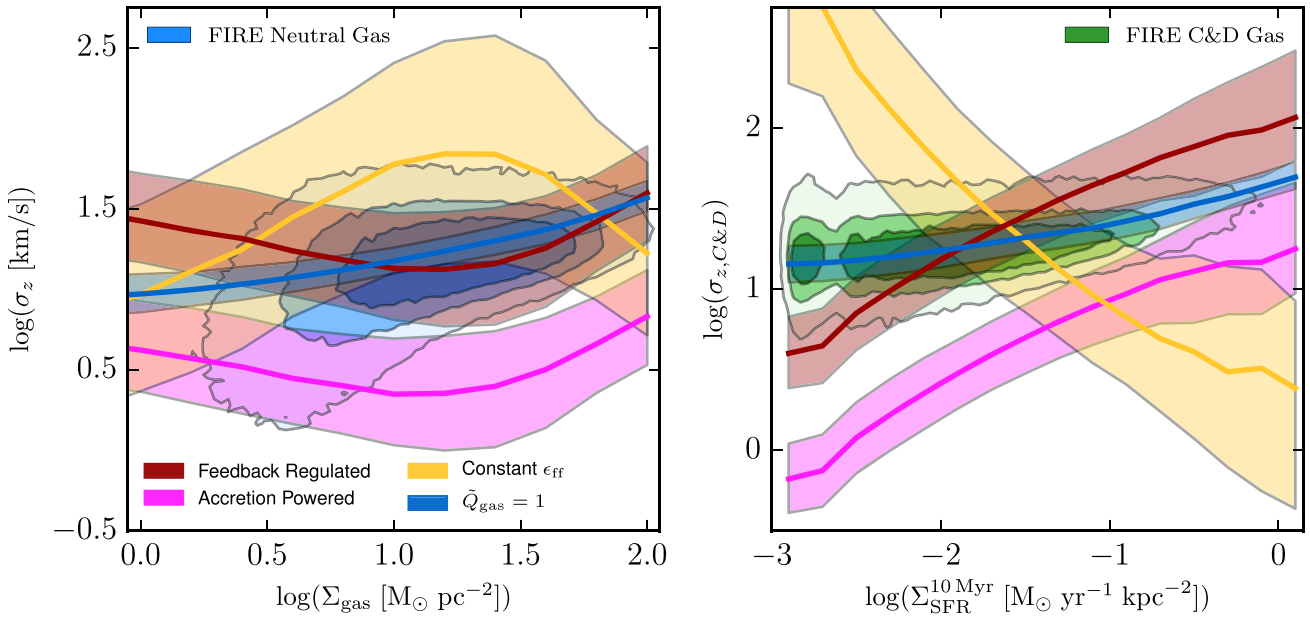

Figure 9. Pixel by pixel predictions of velocity dispersions by 'feedback-regulated' model [cardinal, Section 4.2 (ii)], a 'constant-efficiency per free-fall time' model [gold, Section 4.2 (iii)], assuming $\tilde{Q}_{\rm gas} = 1$ (blue, equation 1), and an 'accretion-powered turbulence' model [magenta, Section 4.2 (iv), with $f = \psi = 1$] compared against actual dispersions in the FIRE simulations (background blue and green shaded contours, style as Fig. 2). In both panels, model shaded regions denote interquartile region (with median as solid line), in bins of $\Sigma_{\rm gas}$ and $\Sigma_{\rm SFR}^{10\,\rm Myr}$. All scalings are calculated and presented with the 10 Myr average star formation rate tracer. Left: Predicted σ_z for star formation models and $\tilde{Q}_{\rm gas} = 1$ versus measured neutral gas σ_z as a function of $\Sigma_{\rm gas}$. The feedback-regulated and $\tilde{Q}_{\rm gas} = 1$ models agree well with the core of the measured gas velocity dispersions, whereas the constant-efficiency and accretion-powered models agree with over- and underprediction velocity dispersions in the gas, respectively. Right: Velocity dispersion–SFR relation, showing both model distributions and the FIRE data set (green shaded contours). Here the different slope scalings of the star formation models with respect to $\Sigma_{\rm SFR}$ are on display: feedback-regulation predicts rising σ with $\Sigma_{\rm SFR}$, whereas constant-efficiency star formation predicts falling dispersions, and is in strong disagreement with the simulations. $\tilde{Q}_{\rm gas} = 1$ falls on top of the FIRE data at all SFRs. $\tilde{Q}_{\rm gas} = 1$ is a closer predictor than either at all σ_z.

parcel of gas is

$$-\frac{{\rm d}E_{\rm grav}}{{\rm d}t} = \frac{GM(<r)m}{{\rm d}t}\left[\frac{1}{r-{\rm d}r} - \frac{1}{r}\right] \approx \frac{GM(<r)m}{{\rm d}t}\frac{{\rm d}r}{r^2} = \frac{mv_{\rm c}^2 v_{\rm r}}{r}\,, \quad (7)$$

where $v_{\rm r} \equiv {\rm d}r/{\rm d}t$ is the radial velocity of that gas parcel. Arguing that some fraction of this energy ψ is deposited into gas turbulence, which is maintained in steady state. We require that the change in turbulent energy due to orbital decay/gas migration is thus $-\psi \dot{E}_{\rm grav} \approx \dot{E}_t \approx m\sigma^3/L_{\rm eddy}$, where $L_{\rm eddy} \sim H \sim \sigma/\Omega$ is the turbulent eddy scale taken to be roughly the disc scale height. Equating the decaying orbital energy with the turbulent energy dissipation:

$$\frac{\psi v_c^2}{r} v_r \approx \sigma^2 \Omega\,. \quad (8)$$

And rearranging for σ, and using $\Omega = v_{\rm c}/r$, yields: $\sigma^2 \approx \psi v_{\rm c} v_{\rm r}$. Regardless of any subsequent connections between turbulent dense gas and star formation, this scaling is central to gravitationally driven (derived from orbital in-spiraling) gas turbulence.

Here we must make the assumptions connecting v_r and star formation.[6] Arguing that the mass flux of gas through turbulent eddy-wide annuli in the disc is $\dot{M}_{\rm in} = 2\pi r H \rho_{\rm gas} v_r = 2\pi r \Sigma_{\rm gas} v_r$, we see that the velocity dispersions scale with $\dot{M}_{\rm in}$ as:

$$\sigma^2 \approx \psi \frac{v_c \dot{M}_{\rm in}}{2\pi r \Sigma_{\rm gas}}\,. \quad (9)$$

In steady state, some fraction of the gas entering the eddy-wide annuli is consumed in star formation, thus $\dot{M}_{\rm in} \approx f\dot{M}_{\rm SFR} = \Sigma_{\rm SFR} 2\pi r H f = \Sigma_{\rm SFR} 2\pi r \sigma f/\Omega$. Substituting in for the SFR, we have:

$$\sigma_{z,AP} \approx f\psi v_c \frac{\Sigma_{\rm SFR}}{\Omega \Sigma_{\rm gas}}\,. \quad (10)$$

Barring the normalization, the accretion-powered scaling for velocity dispersion is identical to that of the feedback-regulated model (equation 5) in terms of $\Sigma_{\rm SFR}/\Omega\Sigma_{\rm gas}$.

4.2.1 *Comparing velocity dispersion models*

Fig. 9 shows the result of using the local surface densities, dynamical times, etc. in the spatially resolved FIRE data to predict the velocity dispersions in the gas using these four models. The predictions are compared against the actual velocity dispersions calculated in the

[6]The correct expression in these order-of-magnitude relations can only be determined in a global steady-state disc model, and could be significant (e.g. introducing factors of $\sim R/H$). However, since this is degenerate with other highly uncertain factors, such as the fraction of gas lost to outflows, the fraction of energy which is isotropized, and the fraction of energy which actually goes into turbulence as opposed to being lost directly to either cooling or outflows, or coherent non-circular motions (e.g. eccentricity or spiral/bar motions) in the plane of the disc, we do not consider it in more detail in this work.

simulations in both the neutral, and cold and dense gas. For the $\tilde{Q}_{\rm gas} = 1$ model, we plot the predicted velocity dispersions in the pixels at their 10-Myr-averaged SFR to see essentially how well Toomre-Q alone describes the gas velocity dispersions in the pixels (it does not have a direct connection to $\Sigma_{\rm SFR}$).

In the left panel, comparing neutral velocity dispersions and gas surface densities in the FIRE simulations with these models, we see that both the feedback-regulated and $\tilde{Q}_{\rm gas} = 1$ models do quite well in predicting the simulated velocity dispersions, whereas the constant-efficiency and accretion-powered models significantly over- and under-shoot the simulations. Interestingly, the scatter seen in velocity dispersions is better reproduced by the feedback-regulated model, compared to the $\tilde{Q}_{\rm gas} = 1$ model, as Ω and local gas fractions do not have the same degree of variance compared with SFRs at any given gas surface density in the simulations.

The right panel of Fig. 9 investigates the model predictions for σ as a function of SFR, compared against the cold and dense gas in FIRE. Here we see the stark difference in scalings between the constant-efficiency star formation model, and all others. Given the inverse-square dependence of σ on SFR, the constant-efficiency model greatly over-predicts (under-predicts) velocity dispersions at low (high) SFRs in significant disagreement with the simulations. We see both how well the $\tilde{Q}_{\rm gas} = 1$ model predicts the dense gas velocity dispersions at all SFRs, and how the feedback-regulated and accretion-powered models scale in unison (modulo their normalizations relative to the strength of feedback ($P/m_\star$) and circular velocities $v_{\rm c}$).

In support of the feedback-regulated model, at high SFRs, as per Section 3.6 and the work of Hayward & Hopkins (2017), it is likely unfair to argue that all of the momentum goes into the velocity dispersions of the cold molecular medium. Rather, some outflowing material or heating of the ISM is warranted, and ought to carry away some of the momentum budget, and this framework naturally then overestimates the velocity dispersion in this regime. On the other hand in this regime, the constant efficiency model significantly under-predicts σ_z, and would most easily be rectified by arguing that $\epsilon_{\rm ff}$ itself scales with $\Sigma_{\rm gas}$ (cf. Grudić et al. 2018).

At the other extreme, for low $\Sigma_{\rm SFR}$, the feedback regulated framework under-predicts σ_z by $\sim$0.5 dex, with the constant efficiency model over-predicting it by about $\sim$1.5 dex. In this case, the picture of the ISM as a purely turbulently supported medium breaks down, and the ISM begins to have significant (but not sufficient) thermal support from the atomic phase ($T \approx 8000$ K, $c_s \approx 6\,{\rm km\,s^{-1}}$). Including the thermal component c_s in quadrature with the turbulent scaling predictions would not significantly affect the prediction of the constant efficiency model, as it predicts hundreds of ${\rm km\,s^{-1}}$ of dispersions at the low end of star formation, but would bring the feedback-regulated model into closer agreement.

Again, as seen in the both panels of Fig. 9, assuming that all gas (whatever its SFR may be) locally has $\tilde{Q}_{\rm gas} = 1$ (equation 1) is perhaps the best predictor of gas velocity dispersion in the cold and dense ISM phase. And so, marginal stability against gravitational fragmentation and collapse must hold primacy over any model of resulting star formation in galaxies.

We explore the issue of degeneracy between the predictions of the feedback-regulated and accretion-powered models with Fig. 10. Given that both models predict σ_z to scale with $\Sigma_{\rm SFR}/\Omega\Sigma_{\rm gas}$, but that the accretion-powered model predicts a linear scaling with $v_{\rm c}$, we plot the neutral gas velocity dispersions in the FIRE simulations against their local values of $\Sigma_{\rm SFR}/\Omega\Sigma_{\rm gas}$, and colour the figure by the average pixel $v_{\rm c}$. We see no statistically significant dependence of σ_z on $v_{\rm c}$, and thus conclude that though gravitational energy

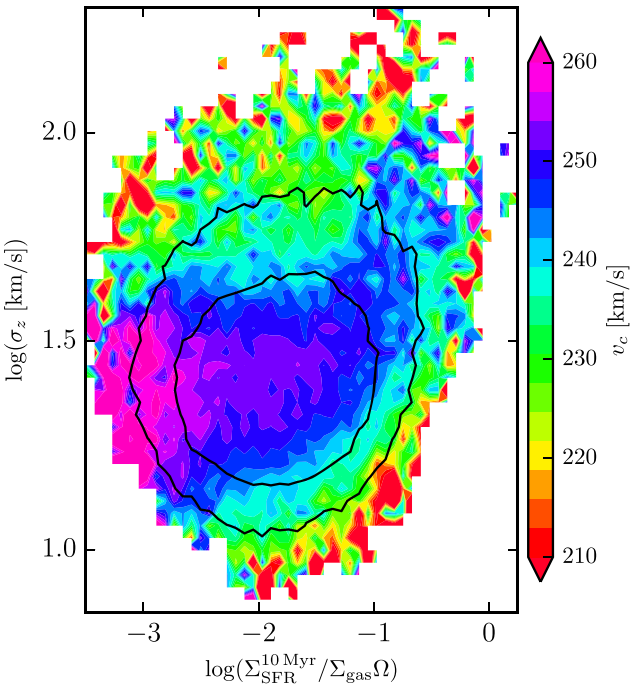

Figure 10. Neutral gas velocity dispersion (in 750 pc pixels) as a function of star formation efficiency in the FIRE simulations, coloured by average circular velocity ($v_{\rm c}$) of pixels. Black contours indicate 75 per cent and 95 per cent data inclusion regions. Both the feedback-regulated (equation 5) and accretion-powered (equation 10) models predict $\sigma \propto \Sigma_{\rm SFR}/\Sigma_{\rm gas}\Omega$. However, the accretion-powered model predicts an additional linear dependence on $v_{\rm c}$ (the feedback-regulated model predicts scaling with the strength of feedback). We see no statistically strong dependence of σ on $v_{\rm c}$, suggesting that gas accretion/migration is a subdominant source of gas turbulence in the FIRE discs.

surely decays into *some* turbulence in the simulations, that it is not the primary source of σ, being subdominant to the effects of feedback or the assumption of marginal gas stability.

Separately, previous work in isolated disc galaxy simulations has shown that simulated discs lacking stellar feedback (in the form of SNe) develop significant anisotropy between in-plane and out-of-plane velocity dispersions, with no-feedback simulations having three to five times less out-of-plane gas motion relative to the in-disc component (Hopkins, Quataert & Murray 2012; Hopkins, Kereš & Murray 2013; Goldbaum, Krumholz & Forbes 2015, 2016). This strongly suggests that orbital decay (i.e. gas accretion) *alone* fails to adequately drive out-of-plane gas motions in discs, owing to the relative difficulty in out-of-plane scattering from in-plane inspiraling alone, and thus necessitating isotropic physical processes (e.g. SNe feedback) to produce the (relatively) isotropic turbulence seen in galaxy discs.

In summary, both the feedback-regulated and $\tilde{Q}_{\rm gas} = 1$ are fairly predictive of the velocity dispersions in gas as a function of SFR in the FIRE Milky Way-like disc galaxies at kpc scales. Accretion-powered turbulence appears to be a subdominant contributor to the overall velocity dispersions in the galaxies at $z \approx 0$, and assuming that star formation proceeds at constant efficiency appear to produce strong disagreement with the velocity dispersions seen in FIRE and observations. Additionally, there are reasonable physical arguments (e.g. accounting for outflows and thermal support) that may help reduce tension at high and low SFRs between the feedback-regulated model. However, these physical effects only

add to the difficulty of the constant-efficiency model in explaining the observed velocity dispersions.

4.3 Effects of inclination on velocity dispersion–SFR relation

Throughout this study, the effects of inclination were avoided by orienting all of simulated galaxies face-on. However, in reality all observed galaxies have some non-zero inclination that must be accounted for. The primary effect of inclination is geometric, where the orbital (in-plane) motion of gas is projected into the line-of-sight measurements *via* 'beam smearing' (Davies et al. 2011). When this occurs, the (orbital) radial velocity gradients are projected into line-of-sight line-widths, and the measured velocity dispersions are artificially increased (see *e.g.* Bassett et al. 2014; Zhou et al. 2017, for their discussions estimating the effect of beam smearing in their data). The effects of beam smearing are largest at small galactocentric radii, as the ratio of pixel size to galactocentric radius grows and velocity curves are rising dramatically, and for larger pixel sizes, as these cases increase the degree of velocity gradient contained within a pixel. In our study, this would generally result in a steeper reported relation between velocity dispersion and SFR, as the highest SFRs (generally) occur at small radii where the effects of beam smearing would be most prominent (and difficult to correct for). The effects of beam smearing can be mitigated somewhat by accurately modeling the orbital motions of the gas, and subtracting that velocity field from the observed data before calculating the line-of-sight line-widths, as well as pushing to higher spatial resolution.

5 SUMMARY AND CONCLUSIONS

In this paper, we explored the properties of the various spatially resolved (250–750 pc scales) line-of-sight gas velocity dispersions, and their relationships with different local SFR tracers and gas properties. These properties were investigated in the context of face-on 'observations' of the Milky Way-mass disc galaxies ($M_\star \approx 10^{10.2}$–$10^{10.9}$ M$_\odot$ at $z \approx 0$) from the Latte suite of FIRE-2 simulations of isolated MW-mass galaxies, and found to be in good agreement with resolved observations of local spiral galaxies. Our principal results are as follows:

(i) Velocity dispersions in neutral (atomic + molecular) gas are nearly constant across 3 dex in 10 Myr average SFRs, distributed between ≈15 and 30 km s^{-1} in our sample of simulated Milky Way-mass spirals (Fig. 2). For both the neutral, and the cold and dense gas velocity dispersions, however, there exists a lower envelope in dispersions as a function of SFR (e.g. on 750 pc scales, we see no gas with $\sigma_z = 20$ km s^{-1} and $\Sigma_{\rm SFR} = 1$ M$_\odot$ yr^{-1} kpc^{-2}).

(ii) In regions with low recent (10-Myr-averaged) SFRs, velocity dispersions correlate with past (100-Myr-averaged) SFRs (Fig. 4). This correlation coincides with the time-scale over which past star formation events will have injected all their feedback momentum into the ISM and driven gas to relative stability ($\tilde{Q}_{\rm gas} \gtrsim 1$).

(iii) The outer contours of the σ_z–$\Sigma_{\rm SFR}$ relation correspond to conditions where the ISM is hosting SFRs (over different time-scales) sufficiently high to expel significant fractions of the ISM as outflows/galactic fountains (Fig. 6). In other words, the ISM can only sustain so much feedback over 10–100 Myr time-scales, without being driven out as outflows/galactic fountains.

(iv) Dense gas depletion times ($\Sigma_{\rm C\&D}/\Sigma_{\rm SFR}^{\rm 10\,Myr}$) are shortest in the cases where either a small fraction of the ISM is dense (thus, nearly all the dense gas is involved in star formation) or where gas surface densities are high and nearly all of the ISM is cold and dense (Fig. 5).

(v) There is evidence for on-off cycles of star formation in the discs (Fig. 8): less gravitationally stable patches of ISM with little past (∼10–100 Myr ago) star formation have the shortest gas depletion times/most vigorous current ($\lesssim$10 Myr) SFRs, and conversely, more gravitationally stable regions with long gas depletion times have had star formation/feedback events in the recent past (10–100 Myr ago).

(vi) The FIRE-2 simulations, and observations, show that regions with higher $\Sigma_{\rm SFR}$ tend to have (albeit weakly) higher σ_z, while models with constant efficiency star formation predict that such regions should have lower σ_z. These simulations and observations are in good agreement with feedback-regulated models that predict SFRs should scale positively with velocity dispersions, and strongly disagree with predictions assuming constant local star formation efficiency.

The velocity dispersion structure of the FIRE Milky Way-mass spirals fits in with our general understanding of gas discs in the turbulently supported framework of disc structure stability. By and large, the dispersions seen and their attendant SFRs are consistent with the feedback-regulated model of star formation (cf. Section 4.2), and marginal gas stability ($\tilde{Q}_{\rm gas} \approx 1$).

The differing time-scales traced by various proxies for SFRs (e.g. Hα fluxes tracing $\lesssim$ 10 Myr versus UV fluxes tracing $\lesssim$ 100 Myr time-scales) and the dynamical times involved for the evolution of turbulent gas line-widths (disc/eddy crossing times) are a frequent difficulty in interpreting studies of velocity dispersions and SFRs in galaxies. However, they also pose a unique opportunity to study the dynamical evolution of the ISM over those time-scales. We have seen evidence in the relative flatness of the σ_z–$\Sigma_{\rm SFR}$ relation for SFRs over 10 Myr time-scales that the ISM can respond relatively quickly in terms of *firing*-up/turning-off star formation compared to the actual driving/decay rate of gas turbulence. Further, in concert with measurements of the current gas stability ($\tilde{Q}_{\rm gas}$), simultaneously using multiple SFR tracers with different time-scales can provide evidence for both feedback regulation time-scales, and vigorous on-off (i.e. bursty) cycles of star formation occurring on ∼10–100 Myr time-scales (at ∼kpc-scales), and differentiate star formation/galaxy disc models.

ACKNOWLEDGEMENTS

MEO is grateful for the encouragement of his late father, SRO, in studying astrophysics, and is supported by the National Science Foundation Graduate Research Fellowship under grant no. 1144469. The authors are grateful to the referee for their comments and providing useful suggestions. The Flatiron Institute is supported by the Simons Foundation. Support for AMM is provided by NASA through Hubble Fellowship grant #HST-HF2-51377 awarded by the Space Telescope Science Institute, which is operated by the Association of Universities for Research in Astronomy, Inc., for NASA, under contract NAS5-26555. Support for PFH was provided by an Alfred P. Sloan Foundation Research Fellowship, NASA ATP grant NNX14AH35G, and NSF Collaborative Research grant #1411920 and CAREER grant #1455342. CAFG was supported by NSF through grants AST-1517491, AST-1715216, and CAREER award AST-1652522, by ⟨0:funding-source 3:href="http://dx.doi.org/10.13039/100000104"⟩NASA⟨/0:funding-source⟩ through grant 17-ATP17-0067, and by a Cottrell Scholar Award from the Research Corporation for Science Advancement. DK acknowledges support

from the NSF Grant AST-1412153 and Cottrell Scholar Award from the Research Corporation for Science Advancement. EQ was supported by NASA ATP grant 12-ATP12-0183, a Simons Investigator award from the Simons Foundation, and the David and Lucile Packard Foundation. AW received support from NASA, through ATP grant 80NSSC18K1097 and HST grants GO-14734 and AR-15057 from STScI, the Heising-Simons Foundation, and a Hellman Foundation Fellowship.

REFERENCES

Bassett R. et al., 2014, MNRAS, 442, 3206
Behroozi P. S., Wechsler R. H., Conroy C., 2013, ApJ, 770, 57
Benincasa S. M., Wadsley J., Couchman H. M. P., Keller B. W., 2016, MNRAS, 462, 3053
Benincasa S. M. et al., 2019, MNRAS, preprint (arXiv:1911.05251)
Bigiel F., Leroy A., Walter F., Brinks E., de Blok W. J. G., Madore B., Thornley M. D., 2008, AJ, 136, 2846
Brinchmann J., Charlot S., White S. D. M., Tremonti C., Kauffmann G., Heckman T., Brinkmann J., 2004, MNRAS, 351, 1151
Cacciato M., Dekel A., Genel S., 2012, MNRAS, 421, 818
Croom S. M. et al., 2012, MNRAS, 421, 872
Davies R. et al., 2011, ApJ, 741, 69
El-Badry K. et al., 2018, MNRAS, 473, 1930
Faucher-Giguere C.-A., Quataert E., Hopkins P. F., 2013, MNRAS, 433, 1970
Gallagher J. S., Hunter D. A., 1983, ApJ, 274, 141
Gallagher M. J. et al., 2018a, ApJ, 858, 90
Gallagher M. J. et al., 2018b, ApJ, 868, L38
Goldbaum N. J., Krumholz M. R., Forbes J. C., 2015, ApJ, 814, 131
Goldbaum N. J., Krumholz M. R., Forbes J. C., 2016, ApJ, 827, 28
Grudić M. Y., Hopkins P. F., Faucher-Giguère C.-A., Quataert E., Murray N., Kereš D., 2018, MNRAS, 475, 3511
Hayward C. C., Hopkins P. F., 2017, MNRAS, 465, 1682
Hopkins P. F., 2015, MNRAS, 450, 53
Hopkins P. F., Quataert E., Murray N., 2012, MNRAS, 421, 3488
Hopkins P. F., Kereš D., Murray N., 2013, MNRAS, 432, 2639
Hopkins P. F., Kereš D., Onorbe J., Faucher-Giguere C.-A., Quataert E., Murray N., Bullock J. S., 2014, MNRAS, 445, 581
Hopkins P. F. et al., 2018, MNRAS, 480, 800
Kennicutt R. C., Evans N. J., 2012, ARA&A, 50, 531
Kennicutt R. C. J., 1989, ApJ, 344, 685
Klessen R. S., Hennebelle P., 2010, A&A, 520, A17
Kroupa P., 2002, Science (80-.)., 295, 82
Kruijssen J. M. D., Longmore S. N., 2014, MNRAS, 439, 3239
Krumholz M., Burkert A., 2010, ApJ, 724, 895
Krumholz M. R., Burkhart B., 2016, MNRAS, 458, 1671
Krumholz M. R., Gnedin N. Y., 2011, ApJ, 729, 36
Krumholz M. R., McKee C. F., Tumlinson J., 2008, ApJ, 689, 865
Krumholz M. R., Dekel A., McKee C. F., 2012, ApJ, 745, 69
Krumholz M. R., Burkhart B., Forbes J. C., Crocker R. M., 2018, MNRAS, 477, 2716
Larson R. B., 1981, MNRAS, 194, 809
Leitherer C. et al., 1999, ApJS, 123, 3
Leroy A. K., Walter F., Brinks E., Bigiel F., de Blok W. J. G., Madore B., Thornley M. D., 2008, AJ, 136, 2782
Leroy A. K. et al., 2013, AJ, 146, 19
Leroy A. K. et al., 2017, ApJ, 846, 71
Ma X., Hopkins P. F., Wetzel A. R., Kirby E. N., Anglés-Alcázar D., Faucher-Giguère C.-A., Kereš D., Quataert E., 2017, MNRAS, 467, 2430
Orr M. E. et al., 2018, MNRAS, 478, 3653
Orr M. E., Hayward C. C., Hopkins P. F., 2019, MNRAS, 486, 4724
Ostriker E. C., Shetty R., 2011, ApJ, 731, 41
Pineda J. L. et al., 2017, ApJ, 839, 107
Querejeta M. et al., 2019, A&A, 625, A19
Rozas M., Sabalisck N., Beckman J. E., Knapen J. H., 1998, A&A, 338, 15
Rozas M., Richer M. G., Steffen W., García-Segura G., López J. A., 2007, A&A, 467, 603
Salim D. M., Federrath C., Kewley L. J., 2015, ApJ, 806, L36
Samuel J. et al., 2020, MNRAS, 491, 1471
Sanderson R. E. et al., 2020, ApJS, 246, 6
Schruba A., Leroy A. K., Walter F., Sandstrom K., Rosolowsky E., 2010, ApJ, 722, 1699
Scott N. et al., 2018, MNRAS, 481, 2299
Simons R. C. et al., 2017, ApJ, 843, 46
Sparre M., Hayward C. C., Feldmann R., Faucher-Giguère C.-A., Muratov A. L., Kereš D., Hopkins P. F., 2017, MNRAS, 466, 88
Sternberg A., Le Petit F., Roueff E., Le Bourlot J., 2014, ApJ, 790, 10
Stilp A. M., Dalcanton J. J., Warren S. R., Skillman E., 2013a, ApJ, 136, 136
Stilp A. M., Dalcanton J. J., Skillman E., Warren S. R., Ott J., Koribalski B., 2013b, ApJ, 773, 88
Sun J. et al., 2018, ApJ, 860, 172
Thompson T. A., Quataert E., Murray N., 2005, ApJ, 630, 167
Toomre A., 1964, ApJ, 139, 1217
Torrey P., Hopkins P. F., Faucher-Giguère C.-A., Vogelsberger M., Quataert E., Kereš D., Murray N., 2017, MNRAS, 467, 2301
Wetzel A. R., Hopkins P. F., Kim J.-h., Faucher-Giguère C.-A., Kereš D., Quataert E., 2016, ApJ, 827, L23
Zhou L. et al., 2017, MNRAS, 470, 4573

APPENDIX: SPATIALLY RESOLVED MAPS AND GAS VELOCITY DISPERSION–SFR RELATIONS OF INDIVIDUAL GALAXY SIMULATIONS

In total, our sample included seven Milky Way-mass disc galaxies from the FIRE-2 suite. Fig. 1 in the main text shows spatially resolved maps of the neutral gas velocity dispersion (σ_z), Toomre-Q ($\tilde{Q}_{\rm gas}$), 100-Myr-averaged gas depletion time ($\Sigma_{\rm gas}/\Sigma_{\rm SFR}^{100\,\rm Myr}$), and star formation 'burst' parameter ($\eta_{\rm burst}$) in two of these galaxies. Fig. A1 shows the remaining five simulated galaxies. Compared to the other disc galaxies, **m12w** is distinct in this sample, both morphologically and having higher velocity dispersions.

Fig. A2 shows the line-of-sight velocity dispersion structure as a function of the 10-Myr-averaged SFR at low redshift, $z \lesssim 0.1$, on 750 pc scales in all seven individual galaxy simulations. Two differently weighted velocity dispersions are plotted: the neutral (atomic + molecular) gas mass-weighted dispersions in (blue) coloured contours, and the 'cold and dense' ($T < 500$ K, $n_H > 1$ cm^{-3}) gas mass-weighted dispersions in unfilled contours. The cold and dense gas dispersions have a very similar structure in σ_z-SFR space, albeit with a lower overall normalization indicative of its dynamically colder state.

By and large, all of the Milky Way-mass spirals (those with the **m12** signifier) show similar structure in dispersion–SFR phase space. There is little variation in the structure of the dispersions across ∼3 dex in SFRs, with the exception of a rising lower envelope in velocity dispersions with SFR. **m12w** stands out with regard to the other simulations in its velocity dispersion structure. However, visually (bottom row, Fig. A1), this galaxy appears morphologically distinct in its gas disc with a ∼3 kpc radius gravitationally fragmenting nuclear gas disc, lacking the ∼10 kpc radial extent of the other simulations at $z = 0$. To a lesser extent, **m12r** also stands out: visually, it has an irregularly structured gas disc at $z = 0$ compared to the other spirals, but does not have as compact a gas distribution as **m12w**. Given the similarity of the apparent physical structure of their discs, and their distributions in σ_z–SFR space, we believe it justified to stack together the pixels from all of the simulation snapshots into a single data set to explore the connections between gas velocity dispersion and local SFR in MW-like disc environments in the main text.

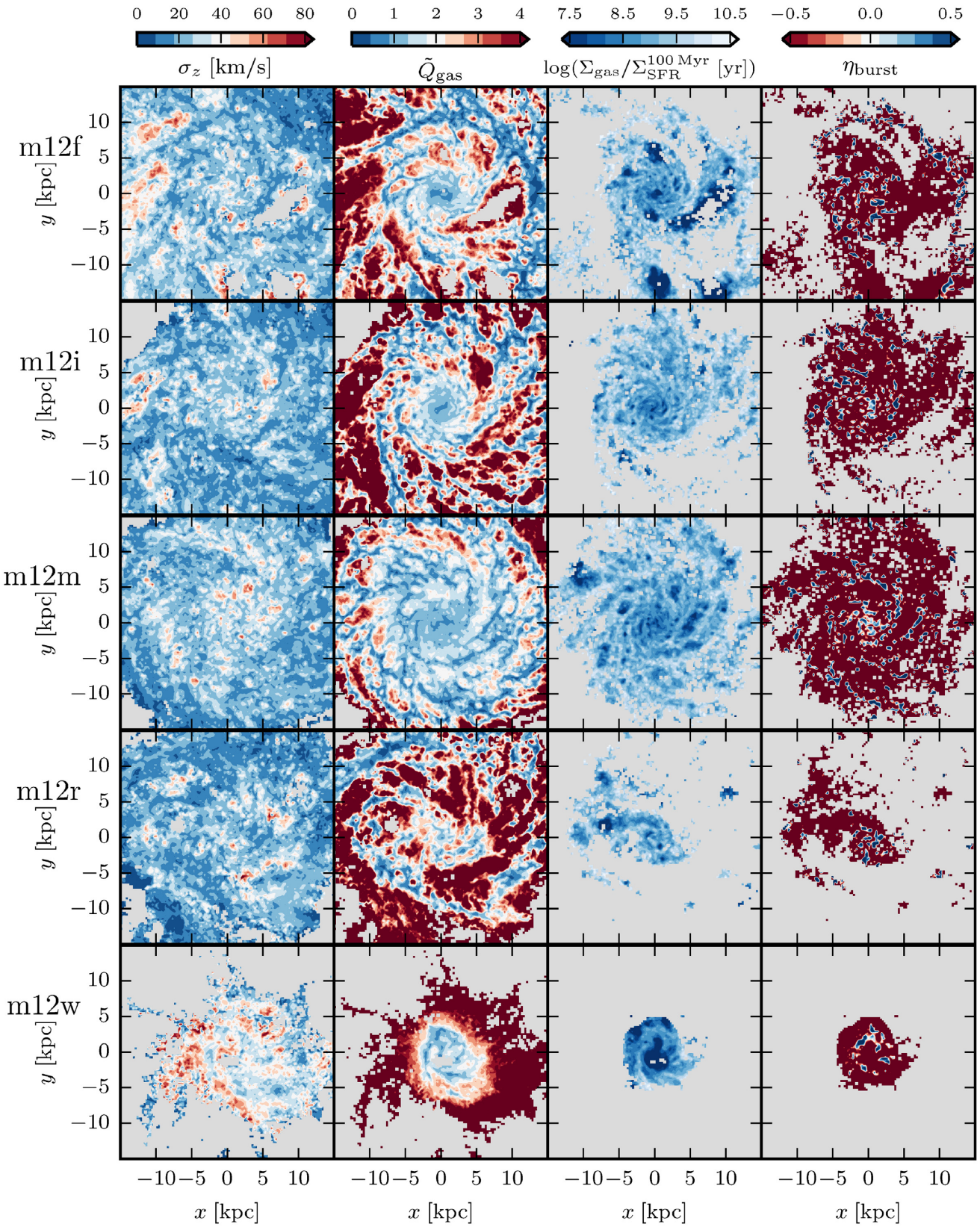

Figure A1. Identical in style and plotted quantities to Fig. 1, but for FIRE simulations: **m12f**, **m12i**, **m12m**, **m12r**, and **m12w** at $z = 0$. Galaxy **m12w** is the least gas rich and most compact in its gas disc of the sample. Unlike the other more extended discs in the sample, **m12w** consists entirely (in gas) of a ∼3 kpc in radius dense, gravitationally unstable, nuclear gas disc.

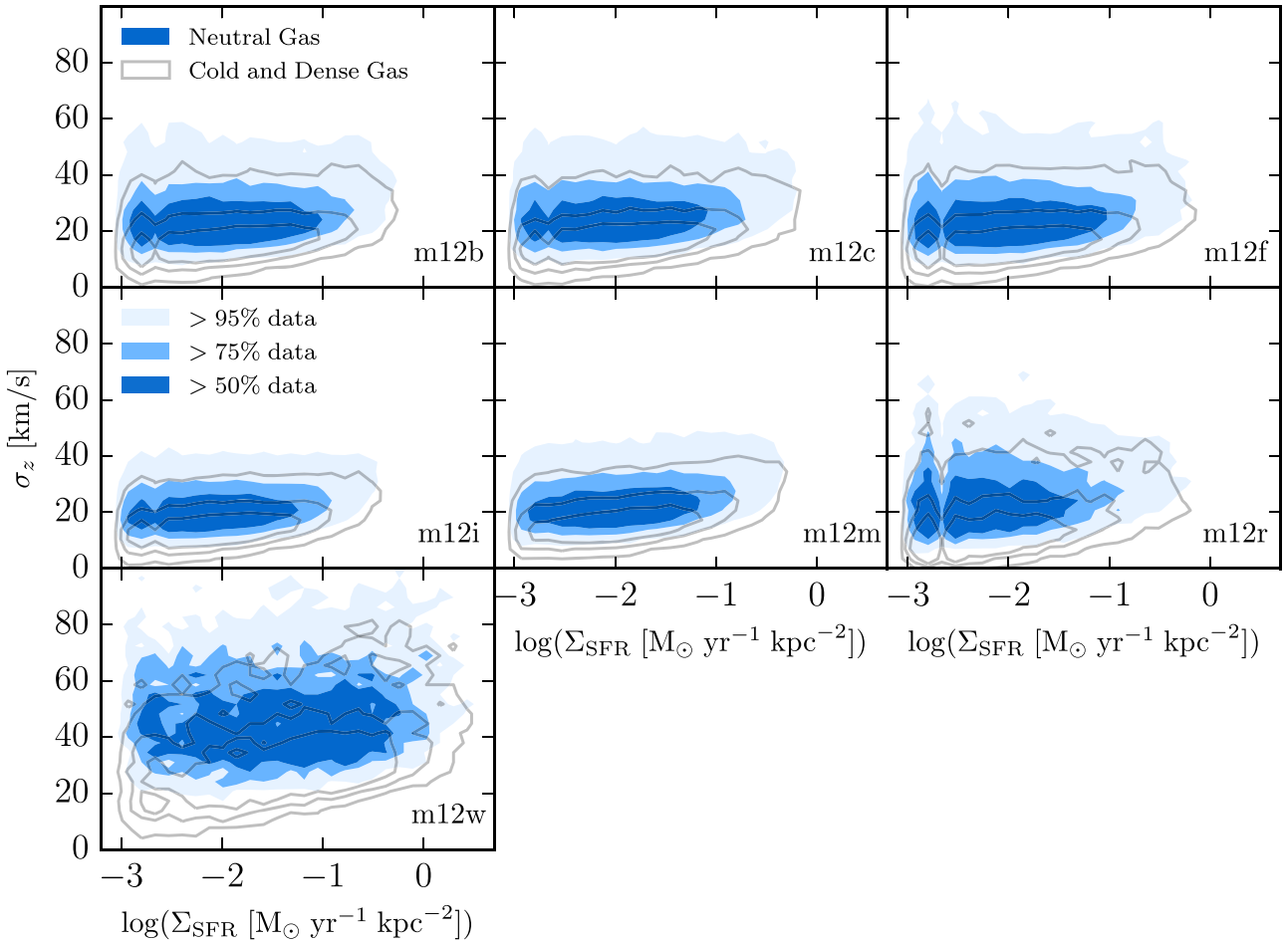

Figure A2. Distributions of spatially resolved (750 pc pixel size) line-of-sight gas velocity dispersions (σ_z) and SFR surface densities for various gas tracers in the FIRE simulations for $z \lesssim 0.1$ (as Fig. 2) in individual FIRE galaxies. Distributions in gas velocity dispersions and SFRs are similar across the individual galaxies, as they are all representative of face-on MW-like disc galaxies. **m12r** and **m12w** represent the most dynamically disturbed disc systems in the core FIRE suite, owing to interactions with their massive LMC-mass satellites near $z \approx 0$, and their higher-σ_z distributions reflect this.

This paper has been typeset from a TEX/LATEX file prepared by the author.